

# Cross-shelf transport of Barents Sea dense water as a sink for atmospheric CO<sub>2</sub> in the Arctic Ocean

**Andreas Rogge** (✉ [andreas.rogge@awi.de](mailto:andreas.rogge@awi.de))

Alfred Wegener Institute Helmholtz Centre for Polar and Marine Research (AWI) <https://orcid.org/0000-0002-4036-4082>

**Markus Janout**

Alfred Wegener Institute <https://orcid.org/0000-0003-4908-2855>

**Nadezhda Zakharova**

Otto Schmidt Laboratory for Polar and Marine Research (OSL), Arctic and Antarctic Research Institute (AARI)

**Emilia Trudnowska**

Institute of Oceanology, Polish Academy of Sciences <https://orcid.org/0000-0003-3471-6632>

**Cora Hoerstmann**

Alfred Wegener Institute Helmholtz Centre for Polar and Marine Research (AWI) <https://orcid.org/0000-0002-0097-2454>

**Claudia Wekerle**

Alfred Wegener Institute Helmholtz Centre for Polar and Marine Research (AWI)

**Laurent Oziel**

Alfred Wegener Institute Helmholtz Centre for Polar and Marine Research (AWI) <https://orcid.org/0000-0001-7939-4011>

**Vibe Schourup-Kristensen**

Aarhus University

**Eugenio Ruiz-Castillo**

Alfred Wegener Institute Helmholtz Centre for Polar and Marine Research (AWI)

**Kirstin Schulz**

Oden Institute for Computational Engineering and Sciences, The University of Texas at Austin

**Vasily Povazhnyy**

Otto Schmidt Laboratory for Polar and Marine Research (OSL), Arctic and Antarctic Research Institute (AARI)

**Morten Iversen**

MARUM & Alfred Wegener Institute <https://orcid.org/0000-0002-5287-1110>

**Anya Waite**

Ocean Frontier Institute and Department of Oceanography, Dalhousie University

---

## Article

### Keywords:

**Posted Date:** June 2nd, 2022

**DOI:** <https://doi.org/10.21203/rs.3.rs-1617794/v1>

**License:**  This work is licensed under a Creative Commons Attribution 4.0 International License.

[Read Full License](#)

**Additional Declarations:** There is **NO** Competing Interest.

---

**Version of Record:** A version of this preprint was published at Nature Geoscience on November 21st, 2022. See the published version at <https://doi.org/10.1038/s41561-022-01069-z>.

1 **Cross-shelf transport of Barents Sea dense water as a sink for atmospheric**  
2 **CO<sub>2</sub> in the Arctic Ocean**

3

4 **Andreas Rogge<sup>1,2</sup>; Markus Janout<sup>2</sup>; Nadezhda Zakharova<sup>3</sup>; Emilia Trudnowska<sup>4</sup>; Cora**  
5 **Hörstmann<sup>2</sup>; Claudia Wekerle<sup>2</sup>; Laurent Oziel<sup>2</sup>; Vibe Schourup-Kristensen<sup>5</sup>; Eugenio**  
6 **Ruiz-Castillo<sup>2</sup>; Kirstin Schulz<sup>6</sup>; Vasily V. Povazhnyy<sup>3</sup>; Morten H. Iversen<sup>2,7</sup>; Anya M.**  
7 **Waite<sup>2,8,9</sup>**

8

9 <sup>1</sup>Institute for Ecosystem Research, Kiel University, Kiel, Germany

10 <sup>2</sup>Alfred Wegener Institute Helmholtz Centre for Polar and Marine Research (AWI),  
11 Bremerhaven, Germany

12 <sup>3</sup>Otto Schmidt Laboratory for Polar and Marine Research (OSL), Arctic and Antarctic Research  
13 Institute (AARI), St. Petersburg, Russia

14 <sup>4</sup>Institute of Oceanology Polish Academy of Sciences, Sopot, Poland

15 <sup>5</sup>Aarhus University, Roskilde, Denmark

16 <sup>6</sup>Oden Institute for Computational Engineering and Sciences, The University of Texas at  
17 Austin, Austin, TX, United States

18 <sup>7</sup>MARUM and University of Bremen, Bremen, Germany

19 <sup>8</sup>University of Bremen FB2 Biology / Chemistry, Bremen, Germany

20 <sup>9</sup>Ocean Frontier Institute and Department of Oceanography, Dalhousie University, Halifax,  
21 Canada

22 **Running title:** Dense water carbon injection

## 23 **Summary**

24 **Export into the deep sea can store significant amounts of atmospheric carbon (C) on**  
25 **millennial time scales, buffering global warming<sup>1,2</sup>. The Barents Sea is one of the most**  
26 **biologically productive areas of the Arctic Ocean<sup>3,4</sup> but C retention times there were**  
27 **thought to be short<sup>5</sup>. Here we show that dense bottom water formation and transport over**  
28 **the continental slope into the deep sea<sup>6-8</sup> result in deep injection of substantial amounts of**  
29 **organic C with long retention times. Observational evidence complemented by numerical**  
30 **model simulations revealed a deep and widespread C injection driven by Barents Sea**  
31 **Bottom Water transport with daily lateral fluxes of  $\sim 2.2$  kt C d<sup>-1</sup> to  $\sim 1200$  m in the Nansen**  
32 **Basin. With increasing distance from the outflow region, the plume expanded and**  
33 **penetrated into even deeper waters, and towards the sediment (retention time hundreds**  
34 **of millennia). Numerical model and genomic data suggest a seasonally fluctuating but**  
35 **continuous transport of C-rich phytoplankton and resuspended material from the**  
36 **Barents and Kara Sea shelves. This mechanism could sequester  $\sim 1/3$  of total C burial**  
37 **across the whole Barents Sea<sup>9</sup>. Our findings combined with those from other export**  
38 **regions of C-rich dense waters in the Arctic<sup>10,11</sup> and around Antarctica<sup>12-16</sup> highlight the**  
39 **importance of lateral transport of bottom water as a C sink globally. Resolving**  
40 **uncertainties around negative feedbacks of global warming due to sea ice decline will**  
41 **necessitate observation of changes in bottom water formation<sup>17</sup> and biological**  
42 **productivity<sup>3</sup> at a resolution high enough to quantify future deep C injection.**

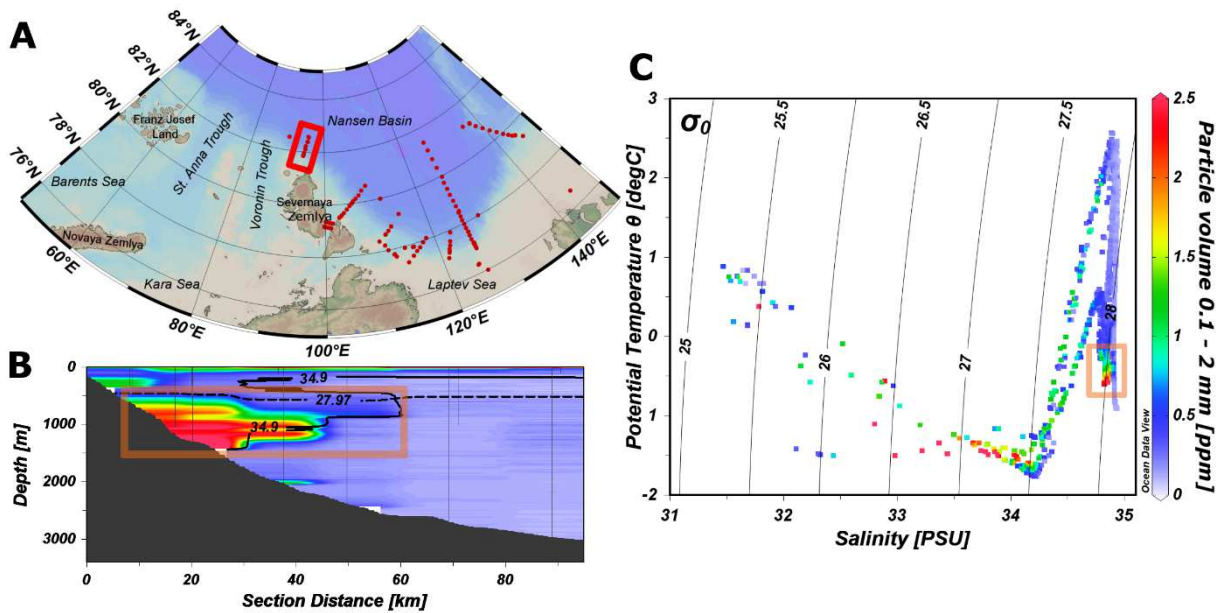
## 43 **Main text**

44 Without the buffering function of the world oceans, the impact of anthropogenic greenhouse  
45 gas emissions would be far more dramatic<sup>2,18</sup>. The oceans' ability to retain up to 25 % of human  
46 CO<sub>2</sub> emissions from the atmosphere<sup>1,19</sup> strongly depends on the local export efficiency and  
47 sequestration depth. Photosynthetically fixed particulate organic carbon (POC) can increase  
48 retention times drastically due to gravitational sinking into deeper water masses or sediments  
49 isolating it from the atmosphere for long time scales<sup>20</sup>. POC fluxes are traditionally considered  
50 to decrease exponentially with increasing depth due to ongoing zooplankton grazing and  
51 zooplankton and microbial respiration<sup>21</sup>. However, a major and yet unconstrained uncertainty  
52 in such vertical decay models is lateral transport, which, if significant, would cause an increased  
53 input of POC at depth and thereby decouple sources and sinks. These processes are rarely  
54 studied and generally not considered in global biogeochemical models. Only a handful of  
55 studies have documented particle injection from productive shelves to the deep sea<sup>22-24</sup>. In  
56 particular polar bottom waters have the potential to carry an important carbon signature into the  
57 deep sea due to density-driven deep vertical integration after entering the ocean basins, but  
58 detailed investigations of this process are missing. The Barents Sea within the Siberian shelf  
59 system is a hotspot of bottom water formation<sup>8,25</sup> and carbon fixation, contributing with appr.  
60 102 Mt C a<sup>-1</sup> <sup>4</sup> about 50 % of the pan-arctic primary production<sup>3</sup>. Due to the lack of detailed  
61 data from the bottom water outflow region, the interplay of both processes and the  
62 consequences for the Arctic and global carbon budget are still not fully resolved. Here we  
63 present results of the multidisciplinary campaign ARCTIC2018 onboard RV Akademik  
64 Tryoshnikov carried out downstream of the outflow area of bottom waters from the productive  
65 Barents Sea shelf in the Nansen Basin and the Laptev Sea. Combining underwater imaging with  
66 water mass and circulation measurements, as well as molecular sequencing techniques and

67 model calculations, we show that bottom water-driven deep carbon injection processes may be  
68 substantial and provide an important pathway for the Arctic carbon sequestration.

### 69 **Bottom water associated lateral particle transport**

70 In August and September 2018 we performed transects of simultaneous vertical high-resolution  
71 profiles within the Nansen Basin east of St. Anna and Voronin Trough (**Fig. 1a**) using a  
72 conductivity, temperature and depth sensor (CTD) equipped with a fluoro- and turbidimeter as  
73 well as an Underwater Vision Profiler camera system (UVP 5hd)<sup>26</sup> to measure particle size-  
74 distribution and abundance. Our data showed a widespread plume of particulate matter in the  
75 Nansen Basin, which was most pronounced north of Severnaya Zemlya (81.9 °N, 94.9 °E - 82.2  
76 °N, 94.9 °E; **Fig. 1**), where the maximum total particle volume for particles larger than 100 µm  
77 (equivalent spherical diameter, ESD) reached 3.5 mm<sup>3</sup> L<sup>-1</sup> (parts per million, ppm). This plume  
78 extended over a vertical area of 19.2 km<sup>2</sup> at depths between 500 and 1200 m and more than 40  
79 km off the shelf and into the Nansen Basin and was co-located with Barents Sea bottom water  
80 (BSBW), defined as practical salinity <34.9 and potential density anomaly >27.97 kg m<sup>-3</sup> (**Fig.**  
81 **1c**). In water depths shallower than 500 m only low particle concentrations, typical for Atlantic  
82 seawater in this region (**Fig. 1b**), were found. Increased concentrations of particles larger than  
83 100 µm observed below were hence transported laterally with the advection of BSBW.



84

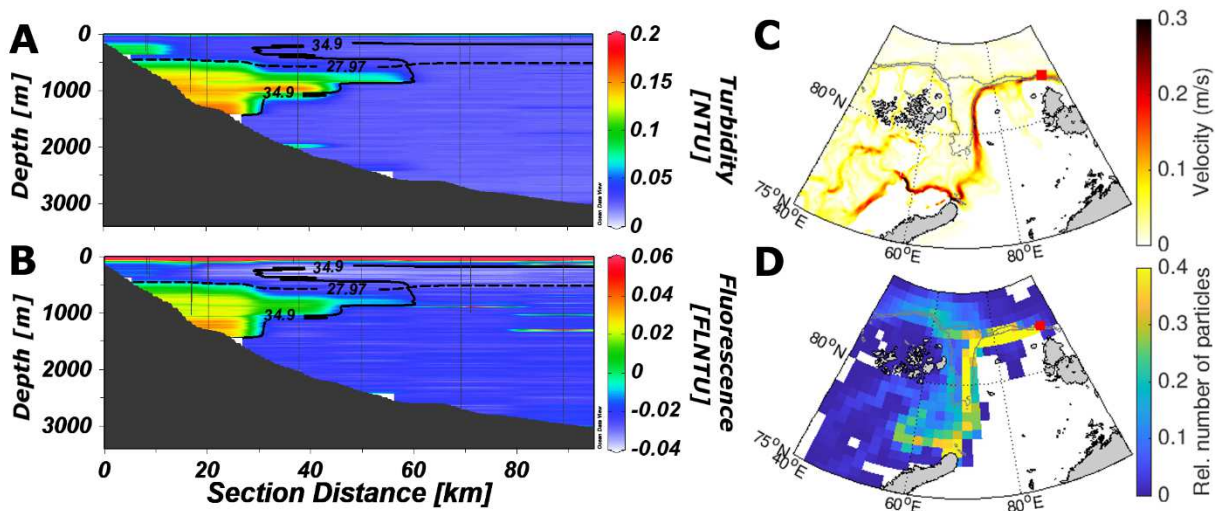
85 **Figure 1: Deep particle plume and its relation to BSBW north of Severnaya Zemlya. a,**  
 86 **Map of the research area including CTD stations (red dots) with the shown transect closest to**  
 87 **the outflow area (red rectangle). b, Spatial particle volume distribution of the size fraction 0.1**  
 88 **– 2 mm (ESD) measured along the transect. Solid (Practical salinity of 34.9) and dashed line**  
 89 **(Potential density anomaly of 27.97 kg m<sup>-3</sup>) indicate BSBW mass boundaries. c, T-S plot with**  
 90 **particle volume as color code show relation of particle maxima with BSBW (orange rectangle**  
 91 **in b and c). Particle volumes have same color bar in b and c.**

92

93 BSBW is formed by successive cooling and brine enrichment of Atlantic Waters of the Barents  
 94 Sea branch caused by sea ice formation on the Barents and Kara Sea shelf<sup>6,8</sup>. It leaves the shelf  
 95 system through St. Anna and Voronin Trough towards the Nansen Basin where it integrates  
 96 into the vertical density gradient below the Atlantic core of the Arctic boundary current. Steered  
 97 by the Coriolis force, BSBW propagates along the shelf break further east towards our study  
 98 area<sup>7,25</sup>.

99 The presence of particles larger than 100 μm ESD mainly in the deeper layers or below the  
 100 BSBW (Fig. 1b, Extended Data Fig. 1b-d) indicated slow gravitational sinking, resulting in a

101 spatial separation during water mass propagation from the outflow regions St. Anna and  
 102 Voronin Trough located several tens of km upstream. Increased turbidity values, that exhibited  
 103 an even higher co-location with BSBW signals (**Fig. 2**), point to a high load of small particles  
 104 still in suspension within this water mass. Especially this material, which is characterized by  
 105 very low sinking velocities, has the potential for long-range lateral transport from shelf regions  
 106 into the deep Nansen Basin.



107  
 108 **Figure 2: Increased turbidity and fluorescence signals within BSBW in the transect north**  
 109 **of Severnaya Zemlya and modeled origin of the material. a, b, Spatial distribution of**  
 110 **turbidity and fluorescence measured along the transect. The area between the solid (Practical**  
 111 **salinity of 34.9) and dashed line (Potential density anomaly of 27.97 kg m<sup>-3</sup>) indicates BSBW.**  
 112 **c, Finite-Element/volume Sea ice-Ocean Model (FESOM)-based calculation of the mean**  
 113 **current velocity at 200 m depth visualizes the main current field of the Barents Sea branch of**  
 114 **the Arctic boundary current. d, Backward trajectories of small non-ballasted particles (0.08 mm**  
 115 **ESD, sinking velocity of 1.03 m d<sup>-1</sup>) calculated with FESOM indicate shelf-based origin of**  
 116 **large fractions even from the northern Barents Sea. Red squares in c and d indicate location of**  
 117 **particle release in the observed plume.**

## 118 **Origin of the material**

119 In order to identify the origin of the particulate material observed within the plume, we  
120 performed reverse particle back-tracking calculations using the Finite-Element/volume Sea ice-  
121 Ocean Model (FESOM<sup>27</sup>, **Extended Data Fig. 2a-c**), which confirmed a lateral injection from  
122 the shelf (**Fig. 2c and d, Extended Data Fig. 2d-g**). Reverse particle trajectories showed that  
123 large fractions of the particle plume North of Severnaya Zemlya originated in the St. Anna  
124 Trough region on the shelf following the main ocean current field into the basin. More than half  
125 of the non-ballasted small particle fraction even originated on average about 750 km upstream  
126 of the observed plume in a region within the northeastern Barents Sea between Novaya Zemlya  
127 and Franz Josef Land (**Extended Data Tab. 1**).

128 The northeastern Barents Sea is a known hotspot of BSBW formation where increased sea ice  
129 formation rates within open waters of lee polynyas cause intense cooling and brine  
130 enrichment<sup>8,25</sup>. Furthermore, enhanced particle production and transport compared to the Arctic  
131 basin is characteristic for this area: Increased light availability within the marginal ice zone and  
132 polynyas in combination with nutrient supply by Atlantic waters, freshwater runoff, and wind-  
133 induced vertical mixing promotes primary productivity<sup>10,28,29</sup>. On the other hand, deep mixing  
134 together with enhanced aggregation leads to high export efficiencies<sup>5,30-32</sup>, whereas strong mean  
135 and tidal currents keep the material in suspension in the frictional bottom boundary layer which  
136 prevents burial on the shelf<sup>33</sup>. This turbulent current regime may also promote resuspension  
137 from the sediment while BSBW is propagating successively towards the outflow troughs.

138 The FESOM simulations included a warm bias of ~1 °C, leading to an underestimation of  
139 BSBW production and therefore also an underestimation of the proportion of particle load  
140 originating from the shallow shelf region. However, several lines of field evidence support the  
141 non-local origin of the observed particles: (1) Genomic analyses of 16S and 18S rRNA gene  
142 amplicon sequencing revealed that the eukaryotic and prokaryotic microbial community

143 differed within the suspended particle fraction  $<100\ \mu\text{m}$  between plume and non-plume  
144 locations (**Extended Data Fig. 3**). Moreover, (2) we identified the benthic indicator species  
145 *Dolichomastigaceae*, recently isolated in deep sea sediments<sup>34</sup>, to be associated with those  
146 particles (**Supplementary Tab. 1**). (3) CTD-based fluorescence signals were increased within  
147 the plume (**Fig. 2b**), pointing towards a phytoplanktonic origin of at least fractions of the  
148 suspended particle load. (4) The majority of marine snow  $>1\ \text{mm}$  associated with the plume  
149 consisted of degraded phytodetritus aggregates as identified in UVP images (**Extended Data**  
150 **Fig. 1e** vs. **Extended Data Fig. 1h-j**). The distinct circular and compact morphology of those  
151 aggregates has recently been described as characteristic for processed aggregates transported to  
152 depth below, especially after Arctic phytoplankton blooms<sup>35</sup>. (5) Abundances of copepods  
153 larger than  $1\ \text{mm}$  ESD were increased within the plume (up to  $50\ \text{ind. m}^{-3}$ , **Extended Data Fig.**  
154 **1g**). UVP images showed copepods to be intact and healthy looking, suggesting that they were  
155 alive and likely actively grazing. Synthesizing this list of field evidence with our back-tracking  
156 model results above, the particle load transported with BSBW can be described as a mixture of  
157 fresh material from the phytoplankton-grazer community within the euphotic shelf zone and  
158 resuspended material from shelf sediments.

159 As a result of this mixed pool of non-local relatively fresh and old material, also size  
160 fractionated elemental C and N analyses revealed contradictory results: Particle samples of the  
161 size fraction  $>100\ \mu\text{m}$  from the BSBW closest the outflow region showed high molar C:N ratios  
162 up to  $>40$  (**Extended Data Fig. 4**) which are typical for old resuspended or even terrigenous  
163 material<sup>36,37</sup>. However, comparable values were also measured for material collected from near-  
164 surface, non-BSBW water samples, but not for the size-fraction smaller than  $100\ \mu\text{m}$  within the  
165 BSBW. Alternatively, the high molar C:N ratios for the large size-fractions could also be caused  
166 by large amounts of extrapolymeric substances, such as polysaccharides within large  
167 phytoaggregates<sup>38</sup>. Since these substances are carbon-rich and nitrogen-poor buoyant particles,  
168 this would have provided a particulate source of carbon that could have caused the high C:N

169 ratios and might also support long distance lateral transport observed in our particle  
170 backtracking results due to reduced sinking velocities.

171

## 172 **Evolution of the particle plume along its propagation pathway**

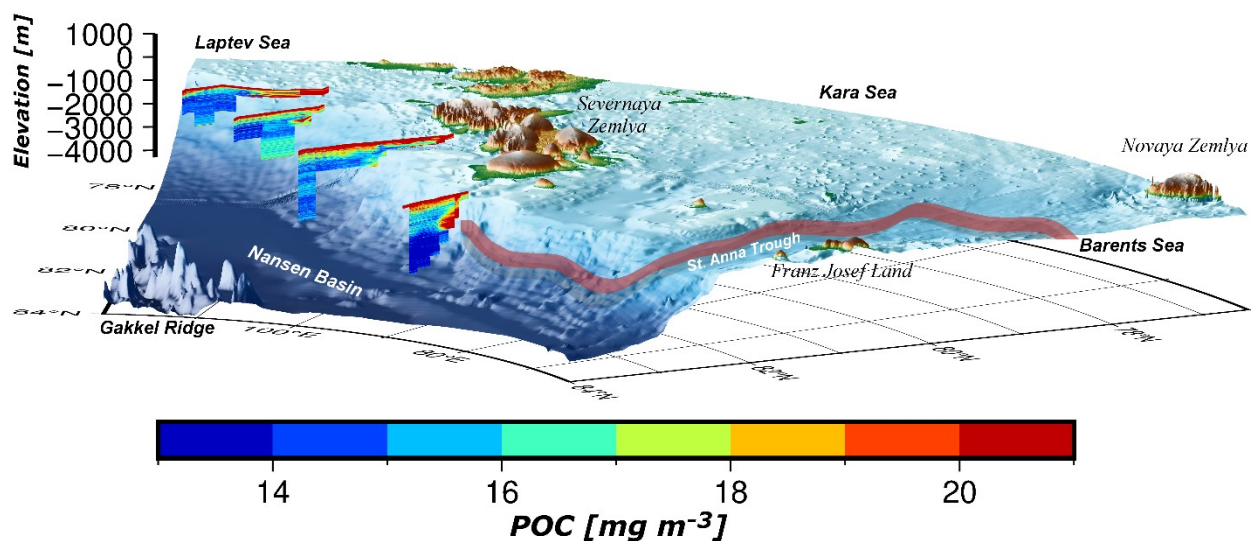
173 In the course of the campaign we could follow the path of BSBW and its particle load further  
174 along the shelfbreak. Approximately 250 km downstream of the first observation, east of  
175 Severnaya Zemlya (103.2 -109.3 °E, 79.5 - 80.5 °N, **Extended Data Fig. 5b & c**), maximum  
176 particle loads reached twice as far into the Nansen Basin (~90 km) but decreased to 2.6 ppm  
177 and were not clearly associated with BSBW. The successive mixing of BSBW with Arctic  
178 bottom water<sup>6,25</sup> decreased BSBW signals whereas particle discharge towards the seafloor  
179 reduced maximum deep particle loads and its association with BSBW with increasing  
180 propagation distance. East of Vilkitzky Strait (78.4 °N, 110.0 °E - 79.3 °N, 114.9 °E, **Extended**  
181 **Data Fig. 5d & e**), ~420 km downstream of the first observation, deep particle load signals  
182 decreased to 1 ppm while the association with decreasing BSBW signatures reduced further.  
183 The ongoing degradation and remineralization, evident in the observations of increased  
184 zooplankton abundances (**Extended Data Fig. 1f**), and the identification of several  
185 heterotrophic indicator species as well as ammonium oxidizing *Nitrococcaceae* in 16S and  
186 18S sequences of particle associated microbes within BSBW (**Supplementary Tab. 1**) further  
187 reduced the POC load and caused discharge of dissolved carbon fractions and nutrients into  
188 surrounding waters. Finally, in the Nansen Basin north of the central Laptev Sea (76.0 °N, 126.0  
189 °E – 81.5 °N, 126.0 °E, **Extended Data Fig. 5f & g**) distinct BSBW signals were absent and  
190 maximum deep particle loads of 0.4 ppm were almost exclusively located below the 27.97 kg  
191 m<sup>-3</sup> isopycnal at around 1500 m. BSBW-driven particle injection thus represents an important  
192 pathway carrying carbon from shelf regions to the deep sea and thereby distributes food and

193 nutrients to the Arctic deep sea community over a distance of 1000 km between St. Anna  
194 Trough and the central Laptev Sea.

195

### 196 **Quantifying BSBW-driven deep carbon injection**

197 To estimate the spatial POC distribution, we scaled up our high resolution UVP, turbidity and  
198 fluorescence data with discrete size-fractionated POC measurements. Based on these  
199 calculations we were able to map the POC distribution within the plume, resulting in maximum  
200 total deep POC concentrations of  $26.5 \text{ mg C m}^{-3}$  north of Severnaya Zemlya (**Fig. 3**). Overall,  
201 the particle size fraction  $<100 \text{ }\mu\text{m ESD}$  contributed about two thirds of the total POC load (on  
202 average  $12.4 \text{ mg C m}^{-3}$  and  $7.0 \text{ mg C m}^{-3}$ , for  $<$  and  $>100 \text{ }\mu\text{m ESD}$ , respectively; **Extended**  
203 **Data Fig. 6**).



204

205 **Figure 3: Spatial distribution of POC estimated based on field measurements.** Red arrow  
206 illustrates the path of particle-loaded BSBW from the Barents Sea shelf through St. Anna  
207 Trough and along the continental slope towards the observed plume.

208 We further estimated the along-slope lateral flux of POC based on the BSBW current velocity  
209 of  $0.06 \text{ m s}^{-1}$  on the day of sampling (i.e. particle and CTD data acquisition) as measured by  
210 Acoustic Doppler Current Profiler (ADCP) and Rotor Current Meter (RCM) within the transect  
211 of the most pronounced plume signals north of Severnaya Zemlya (ERC, Kanzow, T., MJ,  
212 Hölemann, J.: Structure and seasonal evolution of the Arctic Boundary Current off Severnaya  
213 Zemlya. *J Geophys Res* [under review]). Calculations yielded estimates of an average total  
214 lateral carbon flux of  $79.9 - 111.7 \text{ g C m}^{-2} \text{ d}^{-1}$  within the plume ( $<100 \mu\text{m ESD}$ :  $53.8 - 69.1 \text{ g}$   
215  $\text{C m}^{-2} \text{ d}^{-1}$ ,  $>100 \mu\text{m ESD}$ :  $26.1 - 42.8 \text{ g C m}^{-2} \text{ d}^{-1}$ ). Integrated over the vertical BSBW area of  
216  $19.75 \text{ km}^2$  in this transect, we calculated a total lateral transport of  $1.98 \text{ kt C d}^{-1}$ . Including the  
217 POC load from the particles larger than  $100 \mu\text{m ESD}$ , which were observed to slowly sink out  
218 of the BSBW, would increase the total lateral flux to  $2.23 \text{ kt C d}^{-1}$ . This value is equivalent to  
219  $8.2 \text{ kt CO}_2$ , or in more figurative terms, equivalent to the total  $\text{CO}_2$  emission of a medium-sized  
220 car circling the globe  $>1000$  times (assuming an emission of  $19 \text{ kg CO}_2$  per  $100 \text{ km}$ ). Altogether  
221 this process has the potential to transport up to  $0.81 \text{ Mt C a}^{-1}$  into the deep Arctic basin if  
222 carrying material successively with similar daily flux rates from a permanent POC pool on the  
223 shelf. This value would be about one third of the amount of total POC accumulated across the  
224 whole Barents Sea seafloor ( $2.8 \text{ Mt C a}^{-1}$ )<sup>9</sup>. BSBW-driven carbon injection thus retains  
225 significant amounts of carbon from the atmosphere on millennial time-scales<sup>39</sup> due to the slow  
226 circulation of Arctic deep waters and, in turn, acts as a sink in the carbon cycle.

227

## 228 **Temporal trends and implications for polar carbon budgets**

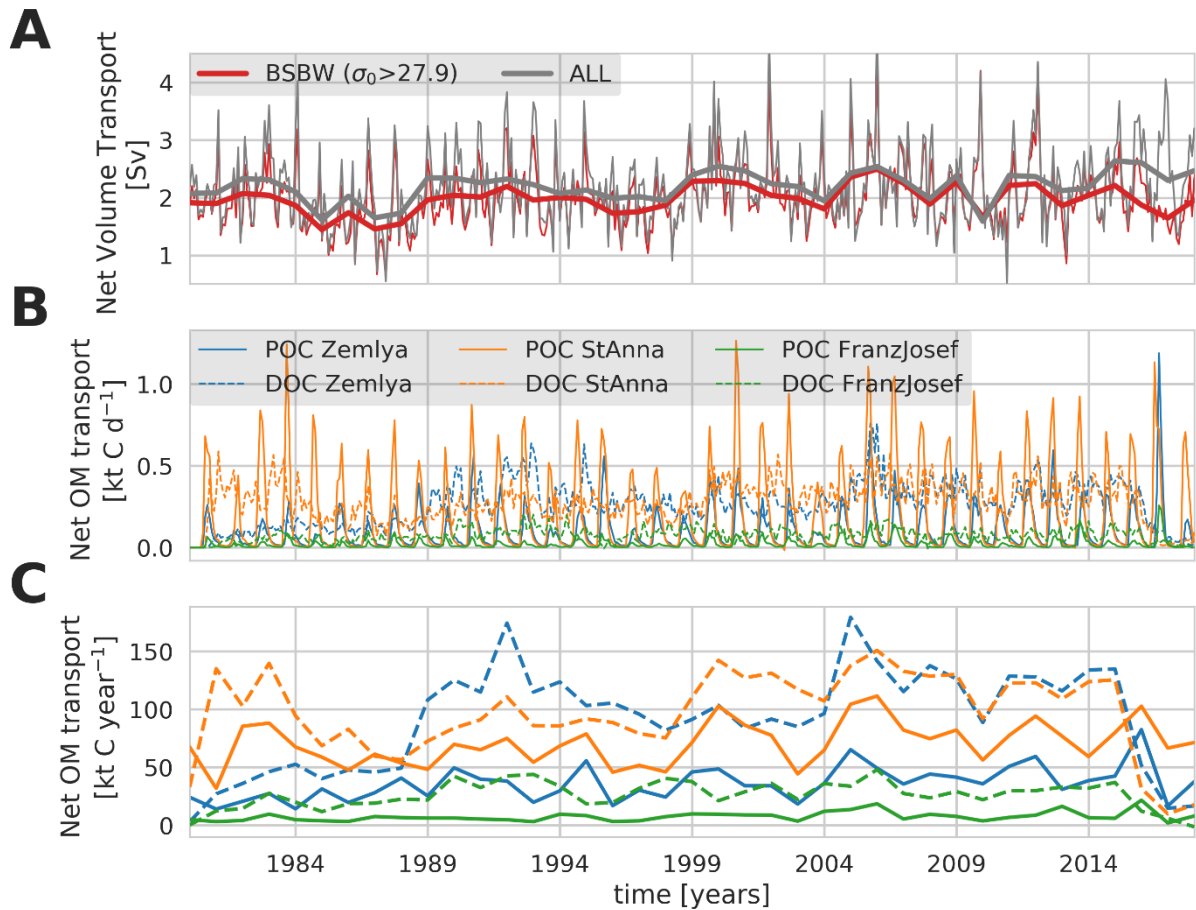
229 Seasonal and inter-annual changes in carbon fixation<sup>9,40</sup> and BSBW production<sup>6,8,17</sup> would be  
230 likely to cause fluctuations of the amount of material injected by BSBW into the deep sea. To  
231 resolve those temporal trends, we performed model calculations using the biogeochemical  
232 Regulated Ecosystem Model (REcoM2<sup>41</sup>) coupled to FESOM. The model was validated by

233 comparing the spatial distribution of POC concentrations from the field with the respective  
234 values in time and space from the model. The model successfully reproduced the process of  
235 dense water formation and subduction driving particle injection. The modelled POC  
236 concentrations associated with subducting dense waters could be found close to the continental  
237 slope north of Severnaya Zemlya (**Extended Data Fig. 7**). However, the location of the  
238 modelled deep POC maximum was ~200 m shallower and POC concentrations were generally  
239 about one order of magnitude lower than the field observations, reaching maximum values of  
240 ~2.5 mg C m<sup>-3</sup> (**Extended Data Fig. 7e vs. g**). This discrepancy could be explained by the  
241 temperature bias in the underlying ocean current model (FESOM, see above), leading to a  
242 reduced density and, hence, a reduced export depth of the produced bottom water as well as a  
243 reduced outflow from the shelf. Additionally, REcoM2 does not include resuspension  
244 processes, which likely play an important role for carbon transport on the shelf (see above) and  
245 might thus lead to underestimations of the transported POC load. These results indicate that the  
246 process of dense water-driven particle injection could qualitatively be well reproduced by  
247 REcoM2 making it a suitable tool to resolve temporal trends of carbon outflow between 2000  
248 and 2018.

249 Model results revealed that pulses of carbon leave the shelf with outflowing dense water (**Fig.**  
250 **4**) and pass our study area north of Severnaya Zemlya every year. These pulses occur during  
251 and following the productive season in the second half of the year (**Fig. 4b**). In the periods  
252 between those peaks, POC outflow almost reaches undetectable levels in the model, but  
253 resuspension of deposited material not represented in the model may cause limited fluxes to  
254 occur in-between bloom phases in reality.

255 Consequently, the model underestimates the POC concentrations (see above) and fluxes by an  
256 order of magnitude compared to our field-based estimates north of Severnaya Zemlya (max.  
257 ~0.08 vs. 0.81 Mt C a<sup>-1</sup>). However, also elevated daily fluxes of dissolved organic carbon

258 (DOC), which were not directly quantified in the field, could be observed in the REcoM2 model  
 259 results (**Fig. 4b**), where annual total DOC fluxes fluctuated between 50 – 200 % of the annual  
 260 POC fluxes (**Fig. 4c**). DOC is known to be transported by polar bottom waters in large  
 261 amounts<sup>42</sup>, which promotes the role of BSBW injection as a significant carbon sink.



262

263 **Figure 4: Time series of cross-sectional transport of water masses and organic carbon**  
 264 **from FESOM and REcoM2 model runs. a**, Total (grey) and BSBW (red) transport through  
 265 St. Anna Trough. **b** and **c**, Daily (**b**) and total annual (**c**) transport of dissolved (dashed lines)  
 266 and particulate (solid lines) organic matter (OM) within BSBW dense water through sections  
 267 North of Franz Josef Land (green), St. Anna Through (orange) and north of Severnaya  
 268 Zemlya (blue).

269 Our FESOM model results revealed a relatively stable annual outflow volume of ~2 Sv of dense  
270 water out of St. Anna Trough between 1980 and 2018 (**Fig. 4a**). During the same period,  
271 REcoM2 results showed the annual lateral POC flux to be slightly increasing within BSBW in  
272 St. Anna Trough (~0.05 to ~0.07 Mt C a<sup>-1</sup>) and within our study area north of Severnaya Zemlya  
273 (~0.025 to ~0.04 Mt C a<sup>-1</sup>). This development could be explained by a higher biological  
274 production due to increased light and nutrient availability as a result of less sea ice cover and  
275 stratification, which was predicted for the northern Barents Sea as a result of global warming<sup>3</sup>.  
276 However, it has also been reported that with ongoing reduction of sea ice cover also the  
277 formation of dense bottom water on the shelf might decrease in the future<sup>17</sup>, which would reduce  
278 the amount and the export depth of carbon sequestered in the Nansen Basin drastically, and in  
279 turn also the retention time. Although, we could not report this scenario in our model runs,  
280 negative feedback effects and hence an amplification of global warming cannot be excluded  
281 because underlying field measurements of carbon and dense water are scarce in this region.

282

## 283 **Conclusions**

284 In this study, we showed that the co-location of bottom water formation and transport with  
285 elevated biological production in the Barents Sea impacts the carbon budget of the Eurasian  
286 Arctic by retaining significant amounts of carbon from the atmosphere in the deep Nansen  
287 Basin. The Barents Sea, however, is not the only shelf region with such a co-location. For  
288 example, polynyas in the Sea of Okhotsk, the Bering Sea and around northern Greenland<sup>10,11</sup>,  
289 but in particular the Antarctic Ross<sup>12</sup> and Weddell Seas<sup>13–15</sup> are characterized by bottom water  
290 formation and transport of organic matter, and it is therefore likely that high dense water  
291 injection rates also occur there as well. Moreover, very high densities of bottom waters  
292 produced around Antarctica<sup>16</sup> can lead to much deeper injection with even longer carbon  
293 retention times than reported here for the Arctic Ocean.

294 Polar Regions are currently changing dramatically and feedback effects of global warming  
295 might lead to even higher global mean temperatures in the future<sup>43</sup>. The scarcity of carbon  
296 measurements in dense water outflow regions leads to uncertainties about the injection system  
297 of the Eurasian Arctic in model simulations. A future reduction of dense water formation and  
298 hence a reduced transport and retention time of carbon from the atmosphere can also be  
299 expected in other polar regions. This might result in a cumulative response and a so far  
300 unconstrained amplification of global warming, which urgently calls for detailed studies of such  
301 systems.

## 302 Main References

- 303 1. Bindoff, N. L. *et al.* Changing Ocean, Marine Ecosystems, and Dependent Communities. In  
304 *IPCC Special Report on the Ocean and Cryosphere in a Changing Climate*, edited by H.-  
305 O. Pörtner, *et al.* (2019).
- 306 2. Hoegh-Guldberg, O. *et al.* Impacts of 1.5°C Global Warming on Natural and Human  
307 Systems. In *Global Warming of 1.5°C. An IPCC Special Report on the impacts of global*  
308 *warming of 1.5°C above pre-industrial levels and related global greenhouse gas emission*  
309 *pathways, in the context of strengthening the global response to the threat of climate*  
310 *change, sustainable development, and efforts to eradicate poverty*, edited by Masson-  
311 Delmotte, V., Zhai, P., *et al.* (2018).
- 312 3. Slagstad, D., Wassmann, P. F. J. & Ellingsen, I. Physical constraints and productivity in the  
313 future Arctic Ocean. *Front. Mar. Sci.* **2**, 311; 10.3389/fmars.2015.00085 (2015).
- 314 4. Arrigo, K. R. & van Dijken, G. L. Continued increases in Arctic Ocean primary production.  
315 *Progress in Oceanography* **136**, 60–70; 10.1016/j.pocean.2015.05.002 (2015).
- 316 5. Reigstad, M., Wexels Riser, C., Wassmann, P. & Ratkova, T. Vertical export of particulate  
317 organic carbon: Attenuation, composition and loss rates in the northern Barents Sea. *Deep*  
318 *Sea Research Part II: Topical Studies in Oceanography* **55**, 2308–2319;  
319 10.1016/j.dsr2.2008.05.007 (2008).
- 320 6. Rudels, B. *et al.* Evolution of the Arctic Ocean boundary current north of the Siberian  
321 shelves. *Journal of Marine Systems* **25**, 77–99; 10.1016/S0924-7963(00)00009-9 (2000).
- 322 7. Dmitrenko, I. A. *et al.* Atlantic water flow into the Arctic Ocean through the St. Anna  
323 Trough in the northern Kara Sea. *J. Geophys. Res. Oceans* **120**, 5158–5178;  
324 10.1002/2015JC010804 (2015).

- 325 8. Ivanov, V. V. & Shapiro, G. I. Formation of a dense water cascade in the marginal ice zone  
326 in the Barents Sea. *Deep Sea Research Part I: Oceanographic Research Papers* **52**, 1699–  
327 1717; 10.1016/j.dsr.2005.04.004 (2005).
- 328 9. Pathirana, I., Knies, J., Felix, M. & Mann, U. Towards an improved organic carbon budget  
329 for the western Barents Sea shelf. *Clim. Past* **10**, 569–587; 10.5194/cp-10-569-2014 (2014).
- 330 10. Tremblay, J.-E. & Smith, W. O. Chapter 8 Primary Production and Nutrient Dynamics in  
331 Polynyas. In *Elsevier Oceanography Series : Polynyas: Windows to the World*, edited by  
332 W. O. Smith & D. G. Barber (Elsevier2007), Vol. 74, pp. 239–269.
- 333 11. Ohshima, K. I., Nihashi, S. & Iwamoto, K. Global view of sea-ice production in polynyas  
334 and its linkage to dense/bottom water formation. *Geosci. Lett.* **3**; 10.1186/s40562-016-0045-  
335 4 (2016).
- 336 12. Arrigo, K. R., van Dijken, G. & Long, M. Coastal Southern Ocean: A strong anthropogenic  
337 CO<sub>2</sub> sink. *Geophys. Res. Lett.* **35**; 10.1029/2008GL035624 (2008).
- 338 13. Huhn, O. *et al.* Evidence of deep- and bottom-water formation in the western Weddell Sea.  
339 *Deep Sea Res Part 2 Top Stud Oceanogr* **55**, 1098–1116; 10.1016/j.dsr2.2007.12.015  
340 (2008).
- 341 14. von Bröckel, K. Primary production data from the south-eastern Weddell Sea. *Polar Biol.*  
342 **4**, 75–80; 10.1007/BF00442903 (1985).
- 343 15. Gleitz, M., Bathmann, U. & Lochte, K. Build-up and decline of summer phytoplankton  
344 biomass in the eastern Weddell Sea, Antarctica. *Polar Biol.* **14**; 10.1007/BF00240262  
345 (1994).
- 346 16. Orsi, A. H., Johnson, G. C. & Bullister, J. L. Circulation, mixing, and production of  
347 Antarctic Bottom Water. *Prog Oceanogr* **43**, 55–109; 10.1016/S0079-6611(99)00004-X  
348 (1999).

- 349 17. Oziel, L., Sirven, J. & Gascard, J.-C. The Barents Sea frontal zones and water masses  
350 variability (1980–2011). *Ocean Sci.* **12**, 169–184; 10.5194/os-12-169-2016 (2016).
- 351 18. Houghton, J. Global warming. *Rep. Prog. Phys.* **68**, 1343–1403; 10.1088/0034-  
352 4885/68/6/R02 (2005).
- 353 19. Watson, A. J. *et al.* Revised estimates of ocean-atmosphere CO<sub>2</sub> flux are consistent with  
354 ocean carbon inventory. *Nat Commun* **11**, 4422; 10.1038/s41467-020-18203-3 (2020).
- 355 20. Ducklow, H. W. & Buesseler, K. O. Upper Ocean Carbon Export and the Biological Pump.  
356 *Oceanography*, 50–58; 10.5670/oceanog.2001.06 (2001).
- 357 21. Martin, J. H., Knauer, G. A., Karl, D. M. & Broenkow, W. W. VERTEX: carbon cycling in  
358 the northeast Pacific. *Deep-Sea Research* **34**, 267–285; 10.1016/0198-0149(87)90086-0  
359 (1987).
- 360 22. Hwang, J., Druffel, E. R. M. & Komada, T. Transport of organic carbon from the California  
361 coast to the slope region: A study of  $\Delta^{14}\text{C}$  and  $\delta^{13}\text{C}$  signatures of organic compound  
362 classes. *Global Biogeochem. Cycles* **19**, n/a-n/a; 10.1029/2004GB002422 (2005).
- 363 23. Waite, A. M. *et al.* Cross-shelf transport, oxygen depletion, and nitrate release within a  
364 forming mesoscale eddy in the eastern Indian Ocean. *Limnol. Oceanogr.* **61**, 103–121;  
365 10.1002/lno.10218 (2016).
- 366 24. Shih, Y.-Y. *et al.* Elevated carbon flux in deep waters of the South China Sea. *Scientific*  
367 *reports* **9**, 1496; 10.1038/s41598-018-37726-w (2019).
- 368 25. Rudels, B. *et al.* Circulation and transformation of Atlantic water in the Eurasian Basin and  
369 the contribution of the Fram Strait inflow branch to the Arctic Ocean heat budget. *Progress*  
370 *in Oceanography* **132**, 128–152; 10.1016/j.pocean.2014.04.003 (2015).

- 371 26. Picheral, M. *et al.* The Underwater Vision Profiler 5. An advanced instrument for high  
372 spatial resolution studies of particle size spectra and zooplankton. *Limnol. Oceanogr.:*  
373 *Methods* **8**, 462–473; 10.4319/lom.2010.8.462 (2010).
- 374 27. Wang, Q. *et al.* The Finite Element Sea Ice-Ocean Model (FESOM) v.1.4: formulation of  
375 an ocean general circulation model. *Geosci. Model Dev.* **7**, 663–693; 10.5194/gmd-7-663-  
376 2014 (2014).
- 377 28. Makarevich, P. R. The primary production of the Barents Sea. *Vestnik MGTU*, 786–793;  
378 10.21443/1560-9278 (2012).
- 379 29. Reigstad, M., Carroll, J., Slagstad, D., Ellingsen, I. & Wassmann, P. Intra-regional  
380 comparison of productivity, carbon flux and ecosystem composition within the northern  
381 Barents Sea. *Progress in Oceanography* **90**, 33–46; 10.1016/j.pocean.2011.02.005 (2011).
- 382 30. Wassmann, P., Slagstad, D., Riser, C. W. & Reigstad, M. Modelling the ecosystem  
383 dynamics of the Barents Sea including the marginal ice zone. *Journal of Marine Systems*  
384 **59**, 1–24; 10.1016/j.jmarsys.2005.05.006 (2006).
- 385 31. Degen, R. *et al.* Patterns and drivers of megabenthic secondary production on the Barents  
386 Sea shelf. *Mar. Ecol. Prog. Ser.* **546**, 1–16; 10.3354/meps11662 (2016).
- 387 32. Shevchenko, V. P., Ivanov, G. & Zernova, V. V. Vertical particle fluxes in the St. Anna  
388 Trough and in the eastern Barents Sea in August-September 1994. In *Modern and Late*  
389 *Quaternary depositional environment of the St. Anna Trough area, northern Kara Sea*,  
390 edited by Reports on Polar Research. 342nd ed. (1999).
- 391 33. Furevik, T. & Foldvik, A. Stability at M 2 critical latitude in the Barents Sea. *J. Geophys.*  
392 *Res.* **101**, 8823–8837; 10.1029/96JC00081 (1996).
- 393 34. Marin, B. & Melkonian, M. Molecular phylogeny and classification of the  
394 Mamiellophyceae class. nov. (Chlorophyta) based on sequence comparisons of the nuclear-

395 and plastid-encoded rRNA operons. *Protist* **161**, 304–336; 10.1016/j.protis.2009.10.002  
396 (2010).

397 35. Trudnowska, E. *et al.* Marine snow morphology illuminates the evolution of phytoplankton  
398 blooms and determines their subsequent vertical export. *Nature communications* **12**, 2816;  
399 10.1038/s41467-021-22994-4 (2021).

400 36. Perdue, E. M. & Koprivnjak, J.-F. Using the C/N ratio to estimate terrigenous inputs of  
401 organic matter to aquatic environments. *Estuar Coast Shelf Sci* **73**, 65–72;  
402 10.1016/j.ecss.2006.12.021 (2007).

403 37. McClelland, J. W. *et al.* Particulate organic carbon and nitrogen export from major Arctic  
404 rivers. *Global Biogeochem Cycles* **30**, 629–643; 10.1002/2015GB005351 (2016).

405 38. Passow, U. Transparent exopolymer particles (TEP) in aquatic environments. *Prog.*  
406 *Oceanogr.* **55**, 287–333; 10.1016/S0079-6611(02)00138-6 (2002).

407 39. Armstrong, C. W. *et al.* Valuing Blue Carbon Changes in the Arctic Ocean. *Front. Mar. Sci.*  
408 **6**; 10.3389/fmars.2019.00331 (2019).

409 40. Sakshaug, E. Biomass and productivity distributions and their variability in the Barents Sea.  
410 *ICES Journal of Marine Science* **54**, 341–350; 10.1006/jmsc.1996.0170 (1997).

411 41. Schourup-Kristensen, V., Sidorenko, D., Wolf-Gladrow, D. A. & Völker, C. A skill  
412 assessment of the biogeochemical model REcoM2 coupled to the finite element sea-ice  
413 ocean model (FESOM 1.3); 10.5194/gmdd-7-4153-2014 (2014).

414 42. Rysgaard, S., Glud, R. N., Sejr, M. K., Bendtsen, J. & Christensen, P. B. Inorganic carbon  
415 transport during sea ice growth and decay: A carbon pump in polar seas. *J Geophys Res*  
416 **112**; 10.1029/2006JC003572 (2007).

417 43. Natali, S. M. *et al.* Permafrost carbon feedbacks threaten global climate goals. *Proc Natl*  
418 *Acad Sci USA* **118**; 10.1073/pnas.2100163118 (2021).

## 419 **Methods**

### 420 **Cruise description and sensor setup**

421 Data and samples were collected during the research campaign ARCTIC2018 in the Laptev and  
422 East Siberian Seas on board RV Akademik Tryoshnikov from August 18<sup>th</sup> to September 29<sup>th</sup>  
423 2018. Conductivity, temperature and depth profiles (CTD; SBE 9plus, Sea-Bird Electronics,  
424 USA) including fluorometer (ECO Fl, Wetlabs, USA) and turbidity data (ECO BB, Wetlabs,  
425 USA) were acquired at each station<sup>44,45</sup>. An Underwater Vision Profiler (UVP 5hd; Hydroptic,  
426 France) was mounted on the CTD frame and acquired particle data and images with a maximum  
427 frequency of 20 Hz during descent.

428 Pre-processing of particle and image data was accomplished using the software Zooprocess<sup>46</sup>  
429 and image classification and validation using the web-based application Ecotaxa and Ecopart<sup>47</sup>.  
430 Images were individually classified with the assistance of machine learning classifiers into  
431 respective groups of living zooplankton and non-living marine snow. Marine snow was further  
432 classified into distinct groups using k-means clustering of PCA coordinates of morphological  
433 features of the detritus images as described by Trudnowska et al.<sup>35</sup>.

434

### 435 **Size fractionated POC/PON sampling and measurements**

436 Size fractionated POC/PON sampling was accomplished by filtering slowly up to 60 L of  
437 sample water directly from the Niskin bottles through 100  $\mu\text{m}$  nylon mesh filters (Millipore).  
438 Subsequently, material  $>100 \mu\text{m}$  on the mesh was rinsed off using sterile filtered sea water (0.2  
439  $\mu\text{m}$ ) and filtered onto 0.8  $\mu\text{m}$  GFF filters (Whatman). 2 L of the corresponding filtrate from 100  
440  $\mu\text{m}$  nylon mesh filters was filtered onto 0.8  $\mu\text{m}$  GFF filters (Whatman) to assess the size fraction  
441  $<100 \mu\text{m}$ . Samples were stored at  $-80 \text{ }^\circ\text{C}$  before removing carbonates by acidification and tin-

442 encapsulation. Measurements of C and N content of the processed samples were carried out  
443 using an element analyzer (Euro EA 3000 Elemental Analyser, Eurovector, Italy).

444

445 **Size fractionated DNA sampling for Amplicon 16S and 18S rRNA gene PCR and**  
446 **sequencing**

447 Size fractionated DNA sampling was accomplished analogously to POC/PON sampling. The  
448 particle size fraction >100 µm ESD was sampled by filtering appr. 10 L of sample water slowly  
449 from the Niskin bottle onto 100 µm nylon mesh (Millipore) before resuspension with sterile  
450 filtered (0.2 µm) sea water and filtration onto 0.22 µm filters (Sterivex™, Millipore) using a  
451 peristaltic pump (Masterflex®, Cole-Parmer, USA). Size fraction <100µm was sampled by  
452 filtering 2 L of the filtrate directly onto 0.22 µm filters. Filters were kept at -80 °C until opening  
453 them in the lab followed by DNA extraction using the DNeasy PowerWater Kit (Qiagen)  
454 according to manufacturer's instructions. The number of the resulting extracts (n) for 16S and  
455 18S sequencing was 24 for the particle size fraction <100 µm and 23 for the size fraction >100  
456 µm, respectively. DNA extracts were stored at -20 °C before generation of prokaryotic and  
457 eukaryotic amplicon sequences targeting the 16S rRNA gene (27F–519R<sup>48</sup>) and 18S rRNA gene  
458 (TA-Reuk454FWD1 – TAREukREV3<sup>49</sup>), respectively. Amplicon libraries were created  
459 following standard protocols of amplicon library preparation (16S Metagenomic Sequencing  
460 Library Preparation, Illumina, Part # 15044223 Rev. B; Appendix B). Both 16S and 18S rRNA  
461 PCR libraries were sequenced using 250-bp paired-end sequencing with a MiSeq Sequencer  
462 (Illumina).

463 **Analyses of amplicon sequence data and statistical analysis**

464 ASV tables were constructed using the DADA2 pipeline v. 1.15.1<sup>50</sup> with standard parameters,  
465 and additional primer trimming using Cutadapt v.1.18<sup>51</sup>. Sequencing statistics for remaining  
466 sequences after each filtering step are reported in **Supplementary Tab. 2** and **Supplementary**  
467 **Tab. 3**. Sequences were taxonomically assigned outside DADA2 using the SilvaNGS v.1.4<sup>52</sup>  
468 pipeline for 16S rRNA gene data with the similarity threshold set to 1. Reads were aligned using  
469 SINA v. 1.2.10<sup>53</sup>, and classified using BLASTn v. 2.2.30<sup>54</sup> with the Silva database v. 132 as a  
470 reference database. 18S rRNA gene amplicons were assigned using the 'feature-classifier'  
471 version 2019.7.0 (from package 'q2-feature-classifier' v. 2019.7.0) in QIIME 2<sup>55</sup> and the pr2  
472 database v. 4.12<sup>56</sup> as a reference database.

473 The ASV tables were Hellinger-transformed to stabilise the variance in the sequence count data  
474 for beta dispersion and PERMANOVA analyses using the decostand() function in  
475 zCompositions (rowsum cutoff = 3). Environmental metadata were z-scored (mean of data  
476 variable shifted to 0) for comparable metadata analysis.

477 To examine microbial community dissimilarity between groups (“outside plume”, “plume”,  
478 “central Vilkitzky”) we performed a principal coordinate analysis (PcoA): we calculated beta  
479 dispersion of sites based on Bray-Curtis dissimilarity analysis of Hellinger-transformed ASV  
480 tables. PCoA eigenvalues were used to examine variation captured in PCoA axes. Differences  
481 of microbial communities between groups were tested with a permutational MANOVA  
482 (PERMANOVA<sup>57</sup>) on the Hellinger-transformed ASV tables using the adonis2() function in  
483 vegan (v.2.5.6).

## 484 **Estimating POC concentration using turbidity, fluorescence and optical particle data**

485 In order to visualize high-resolution POC concentrations and to calculate total POC flux  
486 throughout the bottom water plume, we scaled up size fractionated POC measurements using  
487 CTD-based fluorescence and turbidity data, as well as optical particle concentration and size  
488 distribution data from the UVP. Regressions were carried out using the statsmodels (v0.12.2)  
489 Python module<sup>58</sup>.

490 High-resolution POC concentrations within the UVP size fraction >100  $\mu\text{m}$  ESD were  
491 estimated using the pattern of the relative cumulative particle size distribution, total particle  
492 volume, and POC concentration of the sampled fraction > 100 $\mu\text{m}$  ( $n = 92$ ). The pattern of the  
493 particle size distribution was described by the two coefficients  $a$  and  $b$  of the power law function  
494 ( $f_{(x)} = ax^b$ ) fitted over relative cumulative particle size class proportions using ordinary least  
495 squares (OLS) regression (**see examples in Extended Data Fig. 8a & b**). In order to optimize  
496 fitting, ESDs of size classes are subtracted by the smallest size value (102  $\mu\text{m}$  ESD) to eliminate  
497 the offset below the UVP detection limit. Measured POC concentrations >100  $\mu\text{m}$  ESD were  
498 then correlated to total particle volume up to 2050  $\mu\text{m}$  ESD, as well as the calculated  
499 coefficients  $a$  and  $b$  (**Extended Data Fig. 8c**). The regression was achieved using a generalized  
500 linear model (GLM) based on the gamma distribution model family, logarithmic link function  
501 and iteratively reweighted least squares (IRLS; **Extended Data Table 2**). Resulting intercept  
502 and coefficients were then used to estimate POC concentrations >100  $\mu\text{m}$  for each UVP data  
503 point, following OLS regression of the respective cumulated volumetric particle size  
504 distribution as described above.

505 High-resolution POC estimation of the fraction below the UVP size threshold of 100  $\mu\text{m}$  was  
506 achieved by correlating the POC concentrations of the sampled fraction <100  $\mu\text{m}$  ESD ( $n = 92$ )  
507 with CTD-based turbidity and chlorophyll  $a$  fluorescence sensor data of the respective sampling  
508 location and depth (**Extended Data Fig. 8d**). Therefore, a robust linear regression model

509 (RLM) based on iteratively reweighted least squares (IRLS) including Andrew's Wave M-  
510 estimator as weight function was used (**Extended Data Table 2**). Resulting intercept and  
511 coefficients of this regression were then used to estimate POC concentrations <100  $\mu\text{m}$  ESD  
512 for each CTD data point.

513 Fitting of the resulting estimates of the POC load below and above 100  $\mu\text{m}$  ESD are presented  
514 as the difference between measured and the estimated POC concentration for the respective  
515 sampling location and depth (**Extended Data Fig. 8e**). Almost all larger outliers were located  
516 in the euphotic zone <100 m, pointing towards non-matching locations of sampling and data  
517 acquisition due to the patchiness of the POC distribution in this zone. Nevertheless, about 80  
518 % of the estimates showed a difference below 10  $\text{mg m}^{-3}$ , representing a relatively robust  
519 regression considering the different nature of the approaches, the fact that data acquisition of  
520 CTD and UVP occurred during descent and POC sampling during ascent with wind drift in  
521 between, and that no organisms were picked out of the samples.

522 The overview of estimated POC concentrations in **Fig. 3** was created in PyGMT v.0.6.1<sup>59,60</sup>  
523 using the SRTM15+V2.4 grid<sup>61</sup> and surface gridding<sup>62</sup>.

524

### 525 **BSBW current velocities and data processing**

526 The average ocean current velocity of the area covered by BSBW across the westernmost  
527 transect was estimated from Acoustic Doppler Current Profilers (ADCP's, Teledyne RDI) and  
528 rotor current meters (RCM) deployed in a high-resolution mooring array. The array consisted  
529 of 7 moorings (AK1 to AK7) arranged perpendicular to the continental slope in water depths  
530 between 300 m (AK1) and 3015 m (AK7) from August 2015 to September 2018 (ERC,  
531 Kanzow, T., MJ, Hölemann, J.: Structure and seasonal evolution of the Arctic Boundary  
532 Current off Severnaya Zemlya. *J Geophys Res* [under review]). The sampling frequency for

533 ADCPs and RCMs was 90 and 120 minutes, respectively. The effects of the tide and inertial  
534 periods were removed with a 6-day running average window and temporal resolution was  
535 reduced to one day. Only velocity measurements located within the BSBW region were used  
536 (AK2 to AK5). RCM current records at AK4 and AK5 stopped on 31st of January 2016 and  
537 11th of May 2017, respectively. These gaps in the time series were recovered by scaling  
538 velocities from the ADCPs. Before the current records stopped, correlation between time series  
539 from both instruments for the zonal and meridional components were 0.85 - 0.71 and 0.56 -  
540 0.47 for AK4 and AK5, respectively. Currents from the 20th of August 2018 were aligned in  
541 the along-slope direction and used to represent the time period when the hydrographic transect  
542 was occupied. BSBW was defined by salinities  $<34.9$  and potential density anomalies  $>27.97$   
543  $\text{kg m}^{-3}$ . The area of BSBW was divided accordingly to the location of each mooring and the  
544 depth-average velocity of AK2 and AK3 and the velocities from AK4 and AK5 were combined  
545 with its respective area to estimate the weighted-average velocity of BSBW. More detailed  
546 descriptions of deployment and calculation procedures as well as the resulting data set are  
547 provided in ERC, Kanzow, T., MJ, Hölemann, J.: Structure and seasonal evolution of the Arctic  
548 Boundary Current off Severnaya Zemlya. *J Geophys Res* (under review).

549

#### 550 **Estimating BSBW-driven lateral POC flux in the westernmost transect closest to the St.** 551 **Anna-Trough outflow**

552 BSBW driven lateral POC flux was estimated for the westernmost transect closest to St. Anna  
553 Trough based on POC load estimations described above starting with the station-wise  
554 integration of POC contents within BSBW per  $\text{m}^2$  water column. Potential density anomaly was  
555 calculated by the Thermodynamic Equations Of Seawater – 2010<sup>63</sup> using the Python package  
556 gsw (v. 3.4.0). For each station of this transect, POC contents per  $\text{m}^2$  BSBW per station were  
557 then multiplied by half of the distance to the two nearest stations towards, respectively. No

558 extrapolation towards the south of the southernmost and towards north of the northernmost  
559 station was calculated in order to perform a conservative flux estimation. The resulting POC  
560 content in the whole vertical area of BSBW was then multiplied by the BSBW current velocity  
561 ( $0.06 \text{ m s}^{-1}$ ) within the same transect and from the day of sampling (see above). Finally,  
562 calculation of different time intervals (day, year) and average lateral flux per  $\text{m}^2$  followed.

563 Based on the assumption that a fraction of POC  $>100\mu\text{m}$  ESD was transported into the area by  
564 BSBW but was dislocated due to gravitational settling (see **Fig. 1**, **Extended Data Fig. 1** and  
565 **Extended Data Fig. 6**) one can conclude that this material was also transported with the BSBW  
566 current velocity of  $0.06 \text{ m s}^{-1}$ . In order to obtain estimates of the potential additional fluxes by  
567 this material, we calculated the possible additional POC load as follows: Maximum depth with  
568 increased POC concentration  $> 100 \mu\text{m}$  below BSBW was calculated by identifying the depth  
569 for each station where ambient concentrations below BSBW were reached. Ambient  
570 concentrations were defined for each station as the average POC load  $> 100\mu\text{m}$  in 100 m above  
571 the BSBW subtracted by its standard deviation. Ambient concentrations were reached right  
572 below BSBW in all stations, except for one station located at  $82.11^\circ\text{N}$  and  $94.84^\circ\text{E}$ . For this  
573 profile POC concentrations  $>100 \mu\text{m}$  ESD were integrated over the layer below the depth of  
574 the last BSBW signal and the identified maximum depth. This POC load per  $\text{m}^2$  water column  
575 was then multiplied by half the distances to the next 2 stations north- and southwards as  
576 described above and multiplied by the BSBW current velocity of  $0.06 \text{ m s}^{-1}$ .

577

### 578 **FESOM modelling of current speeds and particle back-tracking**

579 To better understand the velocity structure in the northern Barents Sea, we used the velocity  
580 field from the Finite-Element-Sea ice-Model version 1.4 (FESOM1.4<sup>27</sup>). FESOM1.4 is based  
581 on triangular unstructured meshes for both the ocean and sea ice components. The global  
582 model grid has 4.5 km resolution in the Arctic Ocean and 24 km in the North Atlantic. The

583 model configuration used here was forced with atmospheric reanalysis data from JRA55-do  
584 v.1.3<sup>64</sup> and reasonably represents the hydrography and velocity structure in the Arctic  
585 Ocean<sup>65,66</sup>. One should note that in the model, a known warm bias of around 1°C relative to  
586 the Polar Science Center Hydrographic Climatology (PHC v.3<sup>67</sup>) was present in the Eurasian  
587 Basin of the Arctic Ocean (Figure 4 in Wang et al 2018<sup>65</sup>). Resulting water mass distribution,  
588 however, was similar to field observations, although the location of the dense water plume at  
589 the westernmost transect at ~90 °E was slightly shallower (**Fig. 1 vs. Extended Data Fig. 2** ).  
590 Following release depths for particle back-tracking were adjusted accordingly to match the  
591 observed co-location of particle maxima with dense water.

592 A Lagrangian particle-tracking algorithm was used to determine the origin of particles  
593 observed at the continental shelf break. It has been successfully applied to study the  
594 catchment area of sediment traps deployed in Fram Strait<sup>68</sup>, the pathways of microplastic in  
595 the Arctic Ocean<sup>69</sup>, and vertical microbial connectivity in Fram Strait<sup>70</sup>. 70 particles were  
596 released at the respective depths of bottom water in the model within the westernmost transect  
597 of the plume observed in the field (95°E/ 81.9°N-82.14°N), at 450 m, 500 m, 550 m, 600 m,  
598 650 m, 700 m, and 750 m depth (see **Extended Data Fig. 2c**). Release was carried out every  
599 14 days in 2018 and back-tracked until they reached the ocean surface, resulting in 1680  
600 trajectories. A time step of 30 min was used for the trajectory calculations, yielding bi-hourly  
601 positions. The horizontal displacement of particles was computed with daily-averaged  
602 velocity fields from FESOM1.4, and the vertical displacement was determined from constant  
603 sinking velocities measured for particle samples from Fram Strait<sup>70</sup>. The sinking velocity ( $v$ )  
604 was computed with its empirical relationship to particle ESD described by the coefficients  $a$   
605 and  $b$  of the power law function ( $v = a(\text{ESD})^b$ ). We conducted back-tracking model runs with  
606 sinking velocities representing non-ballasted ( $a = 34.6$ ,  $b = 1.39$ ), small (0.08 mm ESD) and  
607 large (0.5 mm ESD) particles ( $v = 1.03$  and  $13.2 \text{ m d}^{-1}$ , respectively) as well as small ballasted

608 particles ( $a = 94.58$ ,  $b = 0.96$ ) with 0.08 mm ESD ( $v = 8.58 \text{ m d}^{-1}$ ). Selected numerical results  
609 are shown in **Extended Data Tab. 1**.

610

### 611 **Validation of the injection process and seasonal and inter-annual trends using REcoM2**

612 The Regulated Ecosystem Model (REcoM2) is a biogeochemical model describing the lower  
613 trophic levels of the Arctic ecosystem with one zooplankton class, the phytoplankton types  
614 diatoms and nanophytoplankton and one type of detritus<sup>41</sup>. It includes descriptions of the  
615 cycles of nitrogen, silicon and iron as well as the carbon cycle, whereas water mass and  
616 current properties are based on FESOM (see above). The FESOM-REcoM2 setup was run  
617 from 1980 to 2018. The first 25 years of the run have been validated by Schourup-Kristensen,  
618 et al. (2018)<sup>71</sup> while the time-varying trends in Arctic nitrate supply is discussed in LO, VSK,  
619 CW, Hauck, J. The pan-Arctic continental slope as an intensifying conveyor belt for nutrients  
620 in the central Arctic Ocean (1985-2015). *Global Biogeochem Cycles* (submitted).

621 **Data availability**

622 The UVP image and particle data that support the findings is available on EcoTaxa  
623 (<https://ecotaxa.obs-vlfr.fr>, project no. 2463) and Ecopart (<https://ecotaxa.obs-vlfr.fr/part/>;  
624 project no. 239) on request. Results of the PCA based k-means clustering of detritus classes,  
625 depth-binned distributions of zooplankton and particle size classes, as well as the measured  
626 POC/PON data and the resulting POC estimates have been submitted to the PANGAEA data  
627 repository (<https://www.pangaea.de>) and will be publicly available upon publication. CTD data  
628 is available on PANGEA<sup>44</sup> and the Arctic Data Center<sup>45</sup>. Results of the 16S and 18S amplicon  
629 sequencing will be provided on GFBIO (German Federation for Biological Data;  
630 <https://www.gfbio.org/>) upon publication.

631

632 **Code availability**

633 Results were achieved using publicly available Python and R packages as mentioned in the  
634 methods section. However, python scripts, i.e. for POC estimations, can be provided upon  
635 request.

636 **Methods References**

- 637 44. Ivanov, V. Physical oceanography from CTD measurements during Akademik Tryoshnikov  
638 cruise AT2018 to the Arctic Ocean. *PANGAEA - Data Publisher for Earth & Environmental*  
639 *Science*; 10.1594/PANGAEA.905471 (2019).
- 640 45. Polyakov, I. & Rember, R. Conductivity, Temperature, Pressure (CTD) measurements from  
641 cast data taken in the Eurasian and Makarov basins, Arctic Ocean, 2018;  
642 10.18739/A2X34MS0V (2019).
- 643 46. Gorsky, G. *et al.* Digital zooplankton image analysis using the ZooScan integrated system.  
644 *Journal of Plankton Research* **32**, 285–303; 10.1093/plankt/fbp124 (2010).
- 645 47. Picheral, M., Colin, S. & Irisson, J.-O. EcoTaxa, a tool for the taxonomic classification of  
646 images. <http://ecotaxa.obs-vlfr.fr> (2017).
- 647 48. Parada, A. E., Needham, D. M. & Fuhrman, J. A. Every base matters: assessing small  
648 subunit rRNA primers for marine microbiomes with mock communities, time series and  
649 global field samples. *Environmental microbiology* **18**, 1403–1414; 10.1111/1462-  
650 2920.13023 (2016).
- 651 49. Stoeck, T. *et al.* Multiple marker parallel tag environmental DNA sequencing reveals a  
652 highly complex eukaryotic community in marine anoxic water. *Molecular ecology* **19 Suppl**  
653 **1**, 21–31; 10.1111/j.1365-294X.2009.04480.x (2010).
- 654 50. Callahan, B. J. *et al.* DADA2: High-resolution sample inference from Illumina amplicon  
655 data. *Nat Methods* **13**, 581–583; 10.1038/nmeth.3869 (2016).
- 656 51. Martin, M. Cutadapt removes adapter sequences from high-throughput sequencing reads.  
657 *EMBnet Journal*, 10–12; 10.14806/ej.17.1.200 (2011).

- 658 52. Quast, C. *et al.* The SILVA ribosomal RNA gene database project: improved data  
659 processing and web-based tools. *Nucleic acids research* **41**, D590-6; 10.1093/nar/gks1219  
660 (2013).
- 661 53. Pruesse, E., Peplies, J. & Glöckner, F. O. SINA: accurate high-throughput multiple  
662 sequence alignment of ribosomal RNA genes. *Bioinformatics (Oxford, England)* **28**, 1823–  
663 1829; 10.1093/bioinformatics/bts252 (2012).
- 664 54. Camacho, C. *et al.* BLAST+: architecture and applications. *BMC bioinformatics* **10**, 421;  
665 10.1186/1471-2105-10-421 (2009).
- 666 55. Bokulich, N. A. *et al.* Optimizing taxonomic classification of marker-gene amplicon  
667 sequences with QIIME 2's q2-feature-classifier plugin. *Microbiome* **6**, 90; 10.1186/s40168-  
668 018-0470-z (2018).
- 669 56. Guillou, L. *et al.* The Protist Ribosomal Reference database (PR2): a catalog of unicellular  
670 eukaryote small sub-unit rRNA sequences with curated taxonomy. *Nucleic acids research*  
671 **41**, D597-604; 10.1093/nar/gks1160 (2013).
- 672 57. Anderson, M. J. A new method for non-parametric multivariate analysis of variance. *Austral*  
673 *Ecology*, 32–46 (2001).
- 674 58. Seabold, S. & Perktold, J. statsmodels: Econometric and statistical modeling with python.  
675 *9th Python in Science Conference.* (2010).
- 676 59. Uieda, L. *et al.* PyGMT: A Python interface for the Generic Mapping Tools;  
677 10.5281/ZENODO.6426493 (2022).
- 678 60. Wessel, P. *et al.* The Generic Mapping Tools Version 6. *Geochem. Geophys. Geosyst.* **20**,  
679 5556–5564; 10.1029/2019GC008515 (2019).
- 680 61. Tozer, B. *et al.* Global Bathymetry and Topography at 15 Arc Sec: SRTM15+. *Earth and*  
681 *Space Science* **6**, 1847–1864; 10.1029/2019EA000658 (2019).

- 682 62. Smith, W. H. F. & Wessel, P. Gridding with continuous curvature splines in tension.  
683 *GEOPHYSICS* **55**, 293–305; 10.1190/1.1442837 (1990).
- 684 63. IOC, SCOR & IAPSO. *The international thermodynamic equation of seawater – 2010:*  
685 *Calculation and use of thermodynamic properties* (UNESCO (English), 2010).
- 686 64. Tsujino, H. *et al.* JRA-55 based surface dataset for driving ocean–sea-ice models (JRA55-  
687 do). *Ocean Modelling* **130**, 79–139; 10.1016/j.ocemod.2018.07.002 (2018).
- 688 65. Wang, Q., Wekerle, C., Danilov, S., Wang, X. & Jung, T. A 4.5 km resolution Arctic Ocean  
689 simulation with the global multi-resolution model FESOM 1.4. *Geosci. Model Dev.* **11**,  
690 1229–1255; 10.5194/gmd-11-1229-2018 (2018).
- 691 66. Wang, Q. *et al.* Intensification of the Atlantic Water Supply to the Arctic Ocean Through  
692 Fram Strait Induced by Arctic Sea Ice Decline. *Geophys. Res. Lett.* **47**;  
693 10.1029/2019GL086682 (2020).
- 694 67. Steele, M., Morley, R. & Ermold, W. PHC: A Global Ocean Hydrography with a High-  
695 Quality Arctic Ocean. *J. Climate* **14**, 2079–2087; 10.1175/1520-  
696 0442(2001)014<2079:PAGOHW>2.0.CO;2 (2001).
- 697 68. Wekerle, C. *et al.* Properties of Sediment Trap Catchment Areas in Fram Strait: Results  
698 From Lagrangian Modeling and Remote Sensing. *Front. Mar. Sci.* **5**;  
699 10.3389/fmars.2018.00407 (2018).
- 700 69. Tekman, M. B. *et al.* Tying up Loose Ends of Microplastic Pollution in the Arctic:  
701 Distribution from the Sea Surface through the Water Column to Deep-Sea Sediments at the  
702 HAUSGARTEN Observatory. *Environmental science & technology* **54**, 4079–4090;  
703 10.1021/acs.est.9b06981 (2020).

- 704 70. Fadeev, E. *et al.* Sea ice presence is linked to higher carbon export and vertical microbial  
705 connectivity in the Eurasian Arctic Ocean. *Communications biology* **4**, 1255;  
706 10.1038/s42003-021-02776-w (2021).
- 707 71. Schourup-Kristensen, V., Wekerle, C., Wolf-Gladrow, D. A. & Völker, C. Arctic Ocean  
708 biogeochemistry in the high resolution FESOM 1.4-REcoM2 model. *Prog Oceanogr* **168**,  
709 65–81; 10.1016/j.pocean.2018.09.006 (2018).

## 710 **End notes**

### 711 **Acknowledgements**

712 We thank the captain and the crew of the RV Akademik Tryoshnikov and are grateful for UVP  
713 hardware and data assistance by Marc Picheral and the Quantitative Imaging Platform of  
714 Villefranche sur Mer Station Zoologique (PIQv). Thank go to Susanne Spahiç and Nicole  
715 Stollberg for support at sea and Theresa Hargesheimer, Jakob Barz, and Swantje Rogge for  
716 assistance with DNA extraction and amplicon sequencing. AR was funded by the BMBF project  
717 Changing Arctic Transpolar System (CATS, grant number 03F0776E) and CATS-Synthese  
718 (grant number 03F0831D). ET was funded by the Polish Ministry of Science and Education as  
719 Mobility Plus grant (DN/MOB/253/V/2017). Funding for CH was provided in the framework  
720 of the HGF Infrastructure Program POF IV Subtopic 6.2. LO was funded by the European  
721 Union's Horizon 2020 research and innovation programme (project COMFORT, Our common  
722 future ocean in the Earth system – quantifying coupled cycles of carbon, oxygen, and nutrients  
723 for determining and achieving safe operating spaces with respect to tipping points; grant  
724 number 820989) and by the Initiative and Networking Fund of the Helmholtz Association  
725 (Helmholtz Young Investigator Group Marine Carbon and Ecosystem Feedbacks in the Earth  
726 System [MarESys]; grant number VH-NG-1301). VSK was funded by the FRontiers in Arctic  
727 marine Monitoring program (FRAM). Financial support for ERC was provided by the BMBF  
728 project CATS-Synthese (grant number 03F0831B). Financial support for KS was provided by  
729 the NERC-BMBF-funded PEANUTS-project (grant number 03F0804A). MHI was funded by  
730 the DFG-Research Center of Excellence “The Ocean Floor – Earth's Uncharted Interface”:  
731 EXC-2077-390741603 and the framework of the HGF Infrastructure Program FRAM of the  
732 Alfred-Wegener-Institute Helmholtz Center for Polar and Marine Research. Computational  
733 resources for numerical model simulations were made available by the Norddeutscher Verbund  
734 für Hoch- und Höchstleistungsrechnern (HLRN).

735 **Author Contributions**

736 AR performed experimental design, data and sample collection, data preparation, image  
737 validation and analyses, and CN measurements. NZ participated in UVP image validation and  
738 data interpretation. ET performed PCA-based detritus classification. CH performed analyses of  
739 DNA amplicons and PCA-based community differences. ERZ, KS and MJ ran, analysed and  
740 provided ADCP data. CW performed FESOM-based particle back-tracking and current water  
741 mass transport calculations whereas LO and VSK performed biogeochemical REcoM2 model  
742 calculations. AMW, MJ, MHI, and VVP coordinated this study and were involved in  
743 experimental design and data interpretation. AR prepared the manuscript with support and  
744 approval of all co-authors.

745

746 **Competing interests**

747 The authors declare no competing interests.

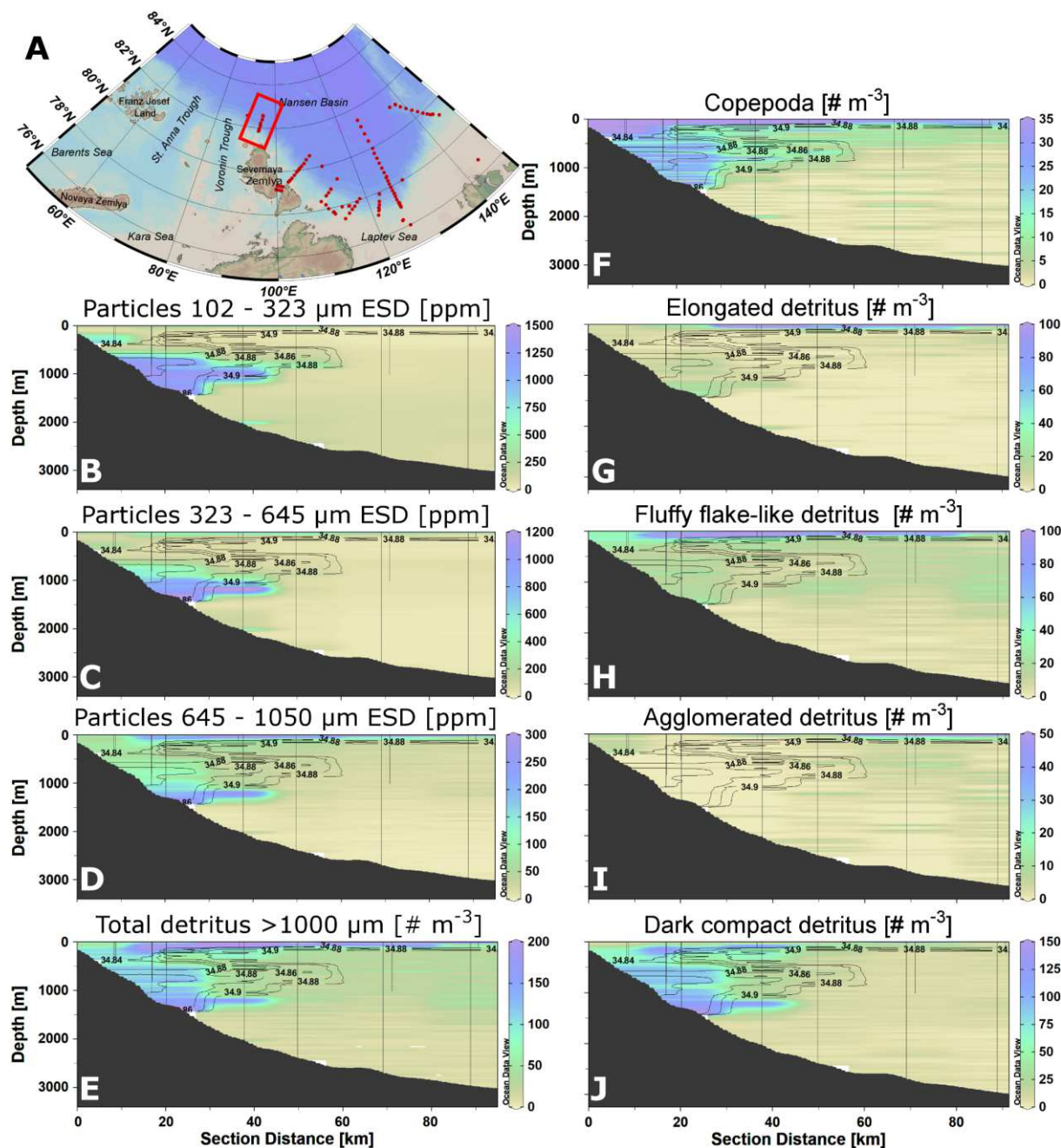
748

749 **Additional Information**

750 Supplementary material is available for this paper. Correspondence and requests for materials  
751 should be addressed to Andreas Rogge (andreas.rogge@awi.de). Reprints and permissions  
752 information is available at [www.nature.com/reprints](http://www.nature.com/reprints).

753 **Extended Data**

754 **Extended Data Figures**



755

756 **Extended Data Figure 1: Detailed results of the UVP-based particle size distribution**

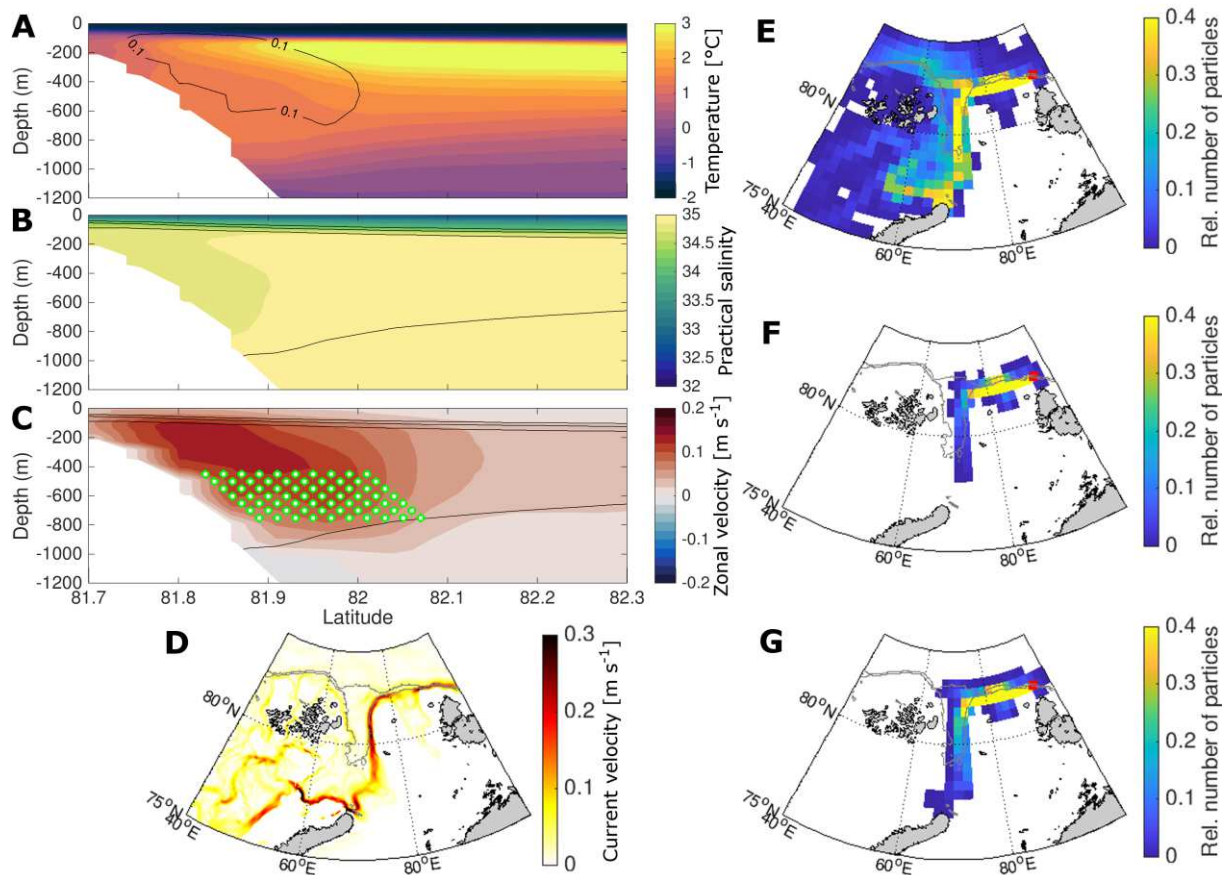
757 **<1050  $\mu\text{m}$  and image analyses >1000  $\mu\text{m}$ . a, map of the research area including stations (red**

758 **dots) and the shown transect (red rectangle) closest to the BSBW outflow region Voronin and**

759 **St. Anna Trough. b - d, spatial distribution of particle size classes <1050  $\mu\text{m}$ . e -f, distribution**

760 **of total detritus > 1000  $\mu\text{m}$  (e), copepods (f), and different detritus classes identified via PCA**

761 **clustering (g-j). Isolines indicate practical salinity. Please note the scale differences.**



762

763 **Extended Data Figure 2: Detailed results of ocean-sea ice modelling (FESOM)-based**

764 **particle back-tracking. a - c, water mass properties (temperature [a] and practical salinity [b])**

765 **and and zonal velocities (c) from FESOM model run for the field transect North of Severnaya**

766 **Zemlya. Green dots in c represent release locations for particle backtracking in dense BSBW.**

767 **d, ocean velocity at 200 m depth-averaged over the years 1989-2018 visualizes the outflow**

768 **from the Barents and Kara Sea shelf through St. Anna Trough. e-g, distribution of different**

769 **particle classes released within the BSBW-plume of our field transect north of Severnaya**

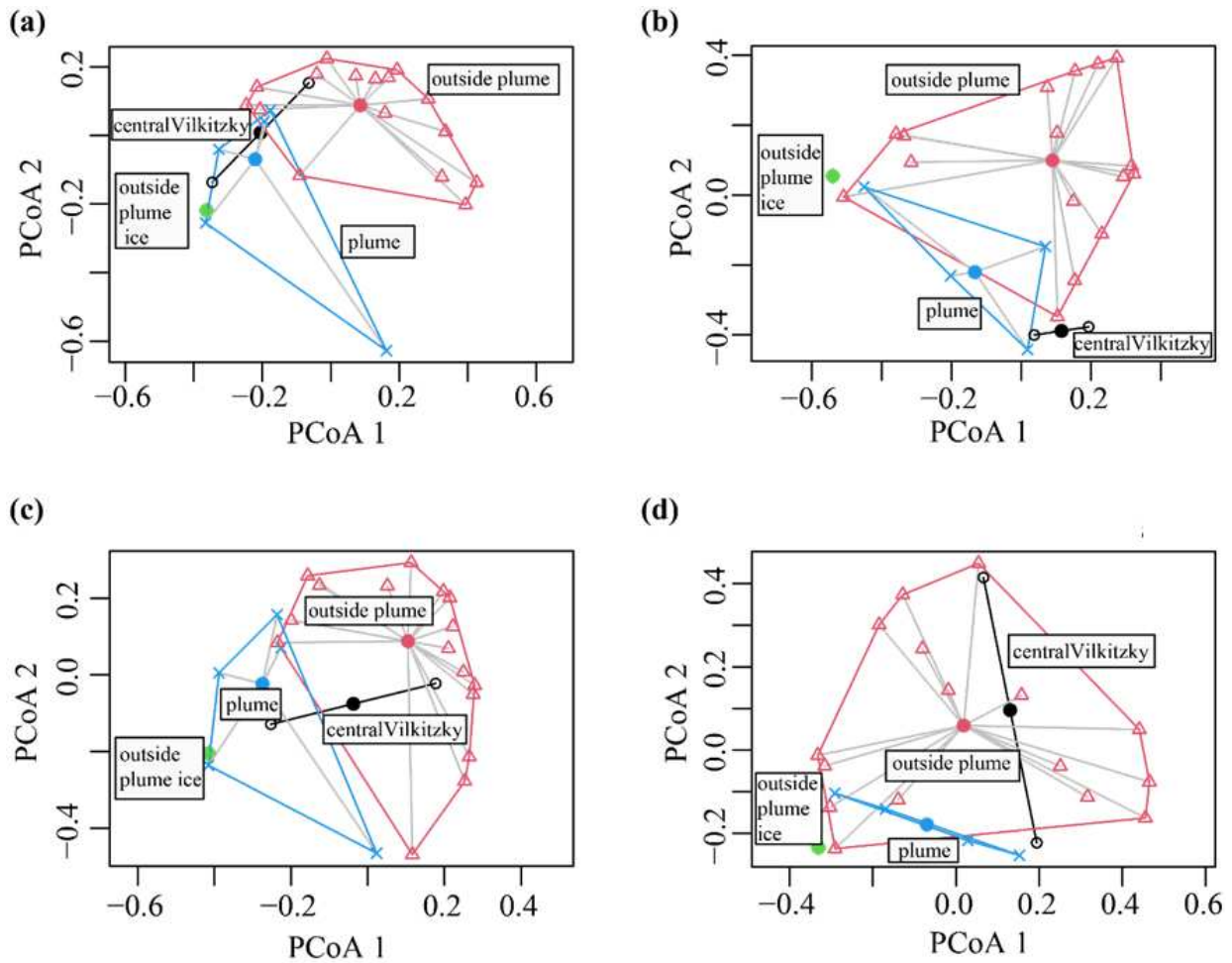
770 **Zemlya (red rectangle) and back-tracked until reaching the surface. e, non-ballasted particles**

771 **with 0.08 mm ESD and a sinking velocity of 1.03 m d<sup>-1</sup>. f, non-ballasted particles with 0.5 mm**

772 **ESD and a sinking velocity 13.2 m d<sup>-1</sup>. g, ballasted particles with small 0.08 mm ESD and a**

773 **sinking velocity of 8.58 m d<sup>-1</sup>. Grey contour lines in d-g indicate the 500 m and 1000 m isobaths,**

774 **respectively.**



775

776 **Extended Data Figure 3: Results of Principal Coordinate Analysis of the particle**

777 **associated community composition. a,** prokaryotic community differences (based on 16S

778 rRNA genes) associated with particles <100 μm ESD. **b,** prokaryotic community differences

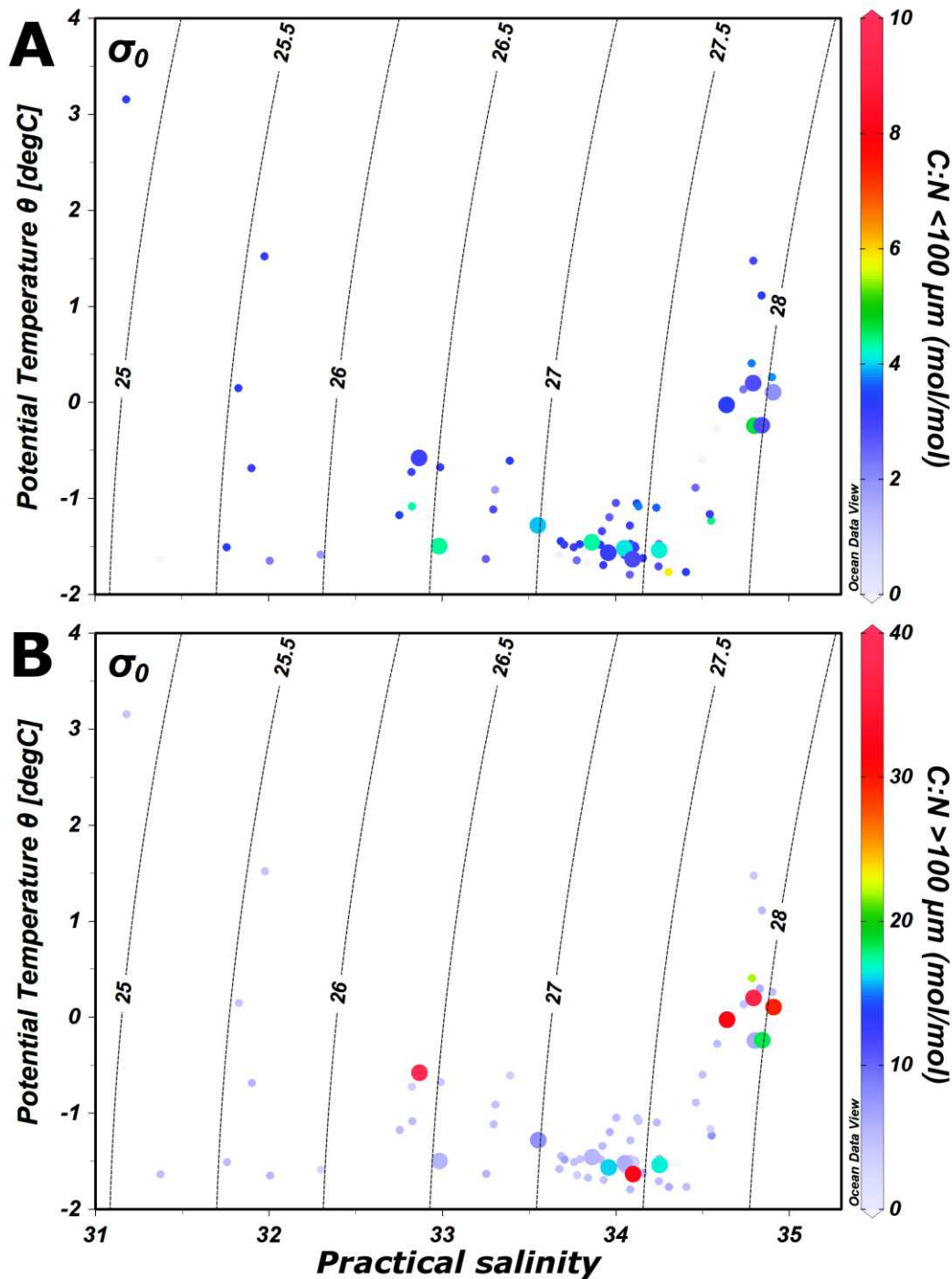
779 (based on 16S rRNA genes) associated with particles >100 μm ESD. **c,** eukaryotic community

780 differences (based on 18S rRNA genes) associated with particles <100 μm ESD. **d,** eukaryotic

781 community differences (based on 18S rRNA genes) associated with particles >100 μm ESD.

782 Significant differences could be identified for the prokaryotic and eukaryotic composition of

783 the microbial community within suspended particles <100 μm ESD.



784

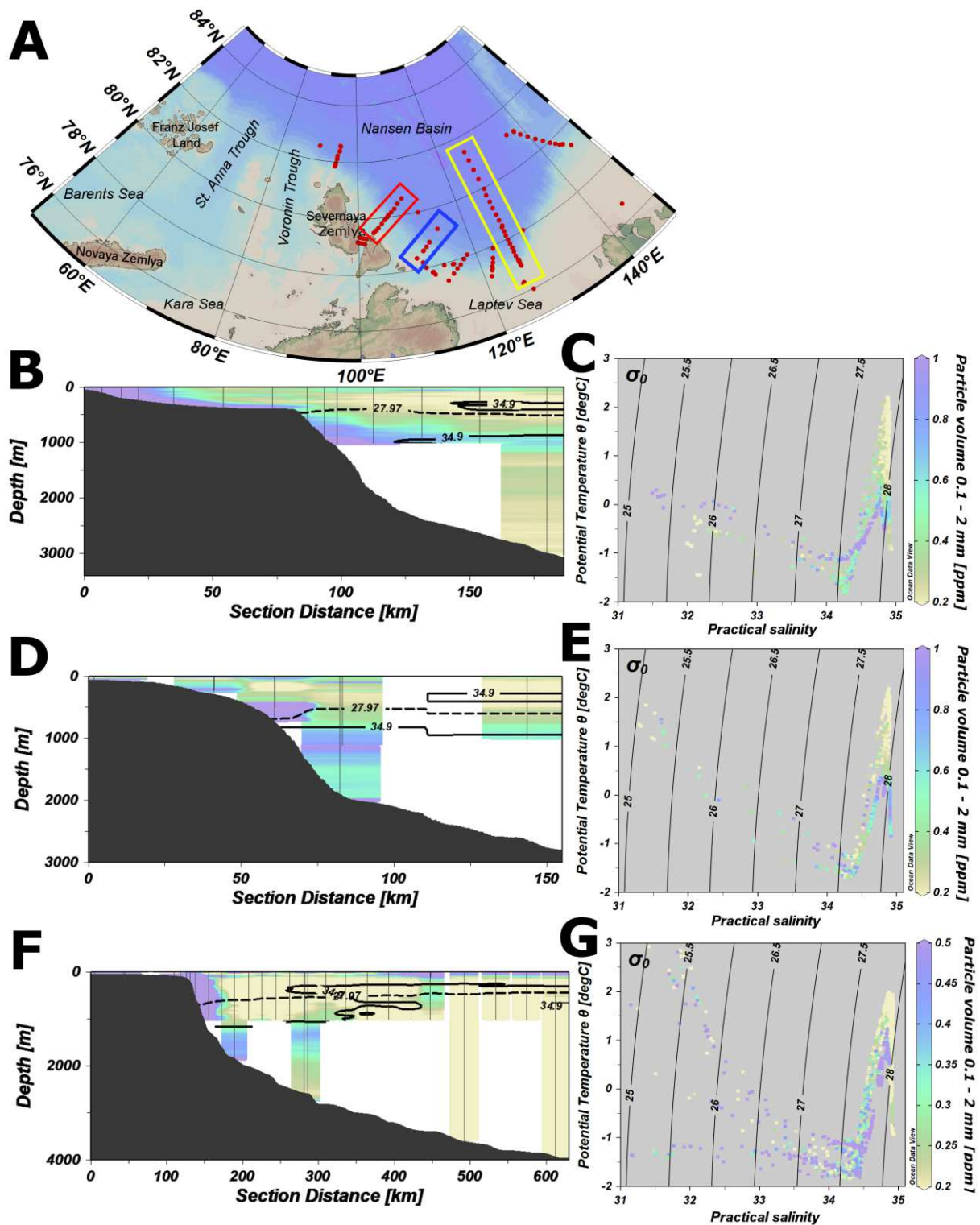
785 **Extended Data Figure 4: Molar carbon to nitrogen ratios depending on temperature and**

786 **practical salinity. a, C:N ratios of the particle size fraction  $<100 \mu\text{m}$ . b, C:N ratios of the**

787 **particle size fraction  $>100 \mu\text{m}$ . Dashed lines indicate isolines of potential density anomaly ( $\sigma_0$ ).**

788 Large dots represent measurements within the transect closest to the BSBW outflow north of

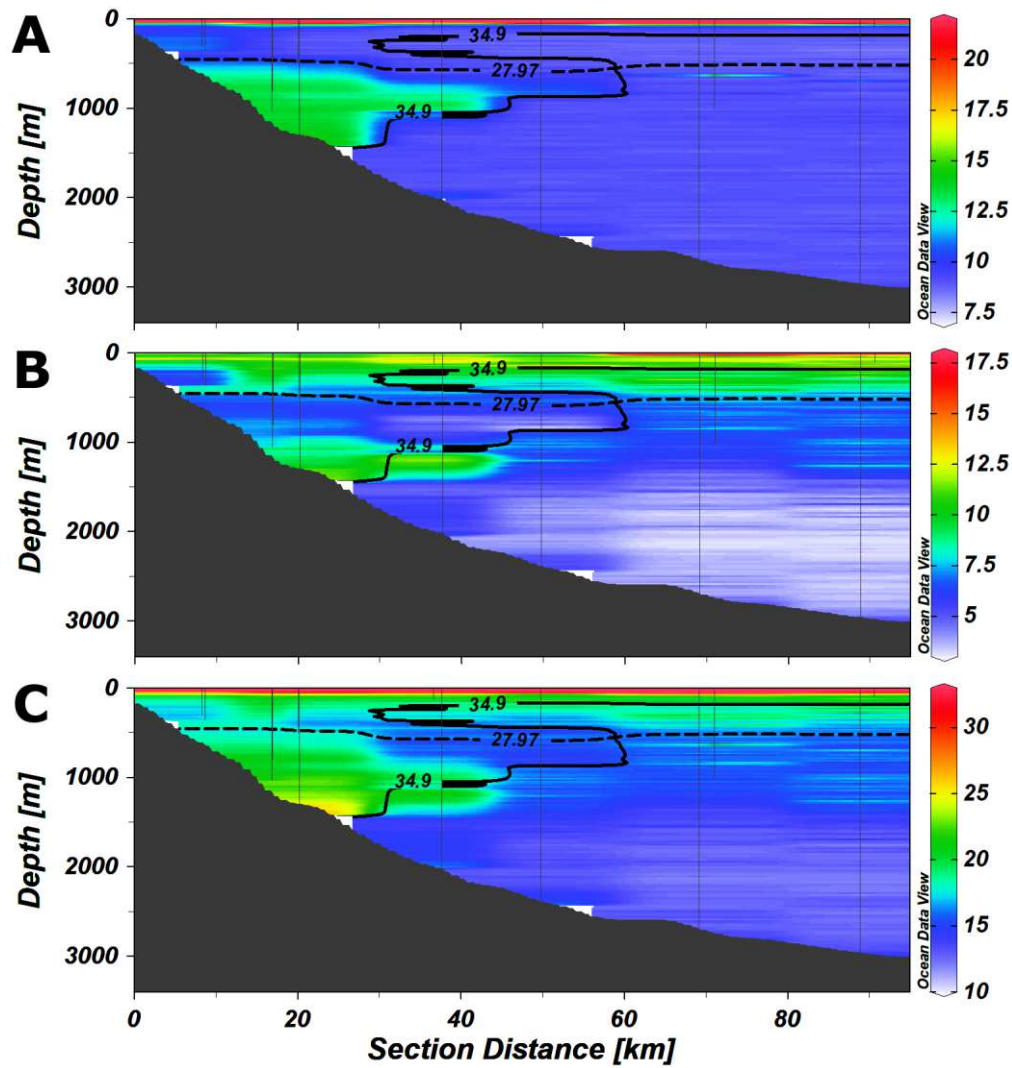
789 Severnaya Zemlya.



790

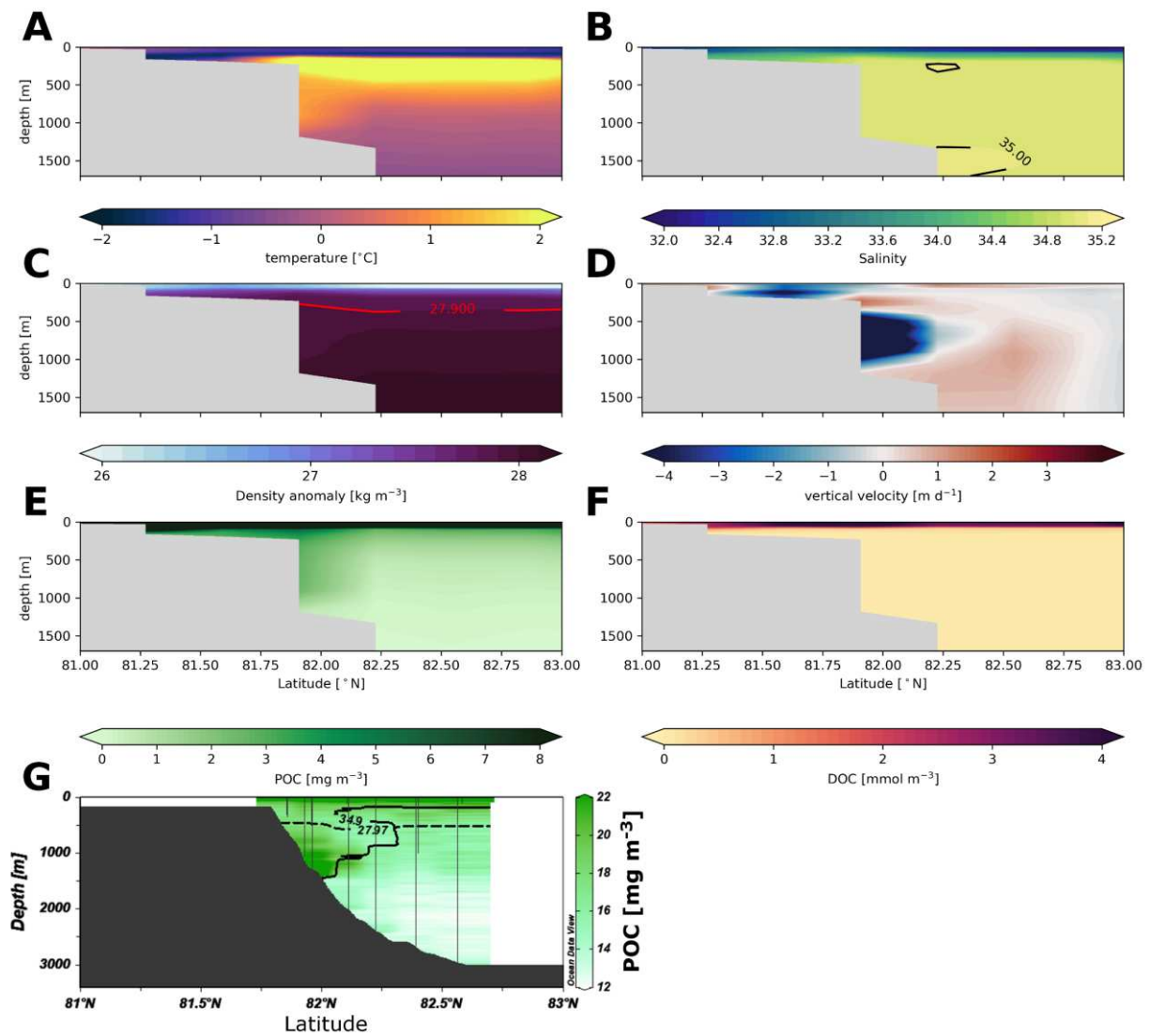
791 **Extended Data Figure 5: Evolution of the deep particle plume and its relation to BSBW**  
 792 **east of Severnaya Zemlya. a, Map of the research area including stations (red dots) and shown**  
 793 **transects in rectangles (red: b, c; blue: d, e; yellow: f, g). b, d, f, spatial particle volume**  
 794 **distribution of the size fraction 0.1 – 2 mm ESD along the respective transect. The areas**

795 between the solid (practical salinity of 34.9) and dashed lines (potential density anomaly of  
796  $27.97 \text{ kg m}^{-3}$ ) indicate BSBW. **c**, **e**, and **f**, Temperature-salinity diagram with color-coded  
797 particle volume shows the relation of particle maxima with BSBW. Black lines indicate isolines  
798 of potential density anomaly ( $\sigma_0$ ). Particle volumes have the same color bar in the respective  
799 transects.



800

801 **Extended Data Figure 6: Sensor-based estimates of the POC distribution north of**  
 802 **Severnaya Zemlya. a**, estimates of POC <100  $\mu\text{m}$  ESD based on reference measurements,  
 803 turbidity and fluorescence sensor data. **b**, estimates of POC >100  $\mu\text{m}$  ESD based on reference  
 804 measurements, and total particle volume and particle size distribution from the UVP. **c**, Total  
 805 POC distribution. The area between the solid (practical salinity of 34.9) and dashed line  
 806 (potential density anomaly of 27.97  $\text{kg m}^{-3}$ ) indicates BSBW.



807

808 **Extended Data Figure 7: Results of REcoM2 runs for the field transect North of**

809 **Severnaya Zemlya and comparison with POC distribution in the field. REcoM outputs for**

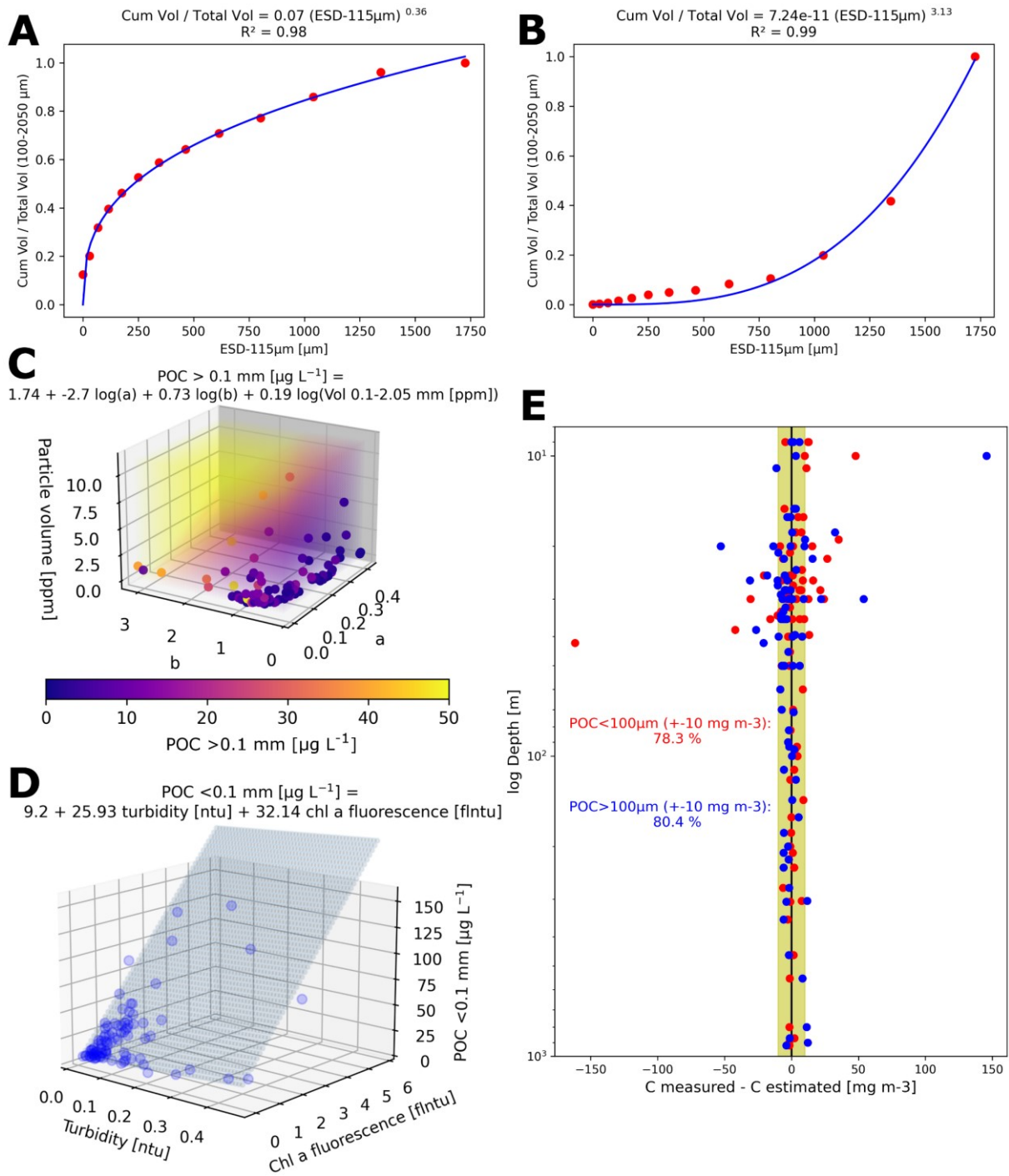
810 August 2018 of: **a**, Temperature ( $^{\circ}\text{C}$ ), **b**, practical salinity, **c**, density anomaly ( $\text{kg m}^{-3}$ ), **d**,

811 vertical velocity ( $\text{m d}^{-1}$ ), **e**, Particulate Organic Carbon ( $\text{mg m}^{-3}$ ), and **f**, Dissolved Organic

812 Carbon ( $\text{mmol m}^{-3}$ ). **g**, total POC concentrations ( $\text{mg m}^{-3}$ ) based on field data estimates. The

813 area between the solid (practical salinity of 34.9) and dashed line (potential density anomaly of

814  $27.97 \text{ kg m}^{-3}$ ) in **g** indicates BSBW.



815

816 **Extended Data Figure 8: Visualization of the sensor based POC estimation. a and b,**

817 examples for power law curve fitting of the relative cumulative particle size distribution

818 between 0.1 – 2.05 mm for one UVP depth bin of 5 m, respectively. c, regression between

819 coefficients (*a*) and exponents (*b*) of the relative cumulative particle size distribution, total

820 particle volume between 0.1 – 2.05 mm, and corresponding measurements of POC >100  $\mu\text{m}$

821 ESD. d, regression between turbidity and chlorophyll *a* fluorescence and corresponding

822 measurements of POC <100  $\mu\text{m}$  ESD. e, Difference between measured concentrations from  
823 samples and estimated POC concentrations for the fraction <100  $\mu\text{m}$  ESD (red) and >100  $\mu\text{m}$   
824 ESD (blue). Golden shade indicates area between -10 and 10  $\text{mg m}^{-3}$ .

825 **Extended Data Tables**

826

827 **Extended Data Table 1: Results of FESOM 1.4 based particle back-tracking**

828

<b>Particle type</b>	<b>Sinking velocity</b>	<b>Fraction of particles originating south of 81 °N</b>	<b>Mean trajectory length of particles originating south of 81 °N</b>	<b>Mean distance between release point and surface of particles originating south of 81 °N</b>
	<b>[m d<sup>-1</sup>]</b>	<b>[%]</b>	<b>[km]</b>	<b>[km]</b>
<b>Non-ballasted 0.08 mm ESD</b>	1.03	50.2	5028	750
<b>Non-ballasted 0.5 mm ESD</b>	13.2	9.9	686	441
<b>Ballasted 0.08 mm ESD</b>	8.58	28.4	835	498

829 **Extended Data Table 2: Descriptions and results of regression models for estimation of**  
 830 **POC concentrations smaller and larger than 100  $\mu\text{m}$  (see also Extended Data Fig. 8).**

**Regression model description for POC <100  $\mu\text{m}$**

<b>Dependent Variable</b>	POC <0.1 mm [ $\mu\text{g L}^{-1}$ ]
<b>Regression model</b>	Robust Linear Model
<b>Weight function</b>	Andrew's wave (tuning constant: 1.339)
<b>Scaling for fitting</b>	median absolute deviation
<b>Link Function</b>	identity
<b>Optimization method</b>	Iteratively reweighted least squares

**Regression results for POC <100  $\mu\text{m}$**

	<b>Coefficient</b>	<b>Standard error</b>	<b>z</b>	<b>P &gt;  z </b>
<b>Intercept</b>	9.1954	1.126	8.164	>0.001
<b>Turbidity [ntu]</b>	25.9341	9.321	2.782	0.005
<b>Chlorophyll a fluorescence [flntu]</b>	32.1410	0.764	42.076	>0.001

**Regression model description for POC >100  $\mu\text{m}$**

<b>Dependent Variable</b>	POC >0.1 mm [ $\mu\text{g L}^{-1}$ ]
<b>Regression model</b>	Generalized Linear Model
<b>Distribution Family</b>	Gamma exponential
<b>Link Function</b>	logarithmic
<b>Optimization method</b>	Iteratively reweighted least squares

**Regression results for POC >100  $\mu\text{m}$**

<b>Log-Likelihood</b>	-292.61			
<b>Deviance</b>	82.685			
<b>Pearson <math>\chi^2</math></b>	98.3			
	<b>Coefficient</b>	<b>Standard error</b>	<b>z</b>	<b>P &gt;  z </b>
<b>Intercept</b>	1.7350	0.263	6.603	>0.001
<b>Particle distribution coefficient a</b>	-2.6996	1.216	-2.220	0.026
<b>Particle distribution coefficient b</b>	0.7251	0.248	2.924	0.003
<b>Total particle volume 0.1-2.05 mm [ppm]</b>	0.1928	0.057	3.389	0.001

## Supplementary Files

This is a list of supplementary files associated with this preprint. Click to download.

- [SIGuide.docx](#)
- [SupplementaryTables.pdf](#)
- [reportingsummary.pdf](#)